1 ***Accelerated viral dynamics in bat cell lines, with implications for zoonotic emergence***

2 Cara E. Brook[1,2†], Mike Boots[1], Kartik Chandran[3], Andrew P. Dobson[2], Christian Drosten[4],

3 Andrea L. Graham[2], Bryan T. Grenfell[2,5], Marcel A. Müller[4,6], Melinda Ng[3], Lin-Fa Wang[7],

4 Anieke van Leeuwen[8,2]

5

6 [1] Department of Integrative Biology, University of California, Berkeley, Berkeley, CA, USA.

7 [2] Department of Ecology & Evolutionary Biology, Princeton University, Princeton, NJ, USA.

8 [3] Department of Microbiology and Immunology, Albert Einstein College of Medicine, Bronx,

9 NY, USA.

10 [4] Institute of Virology, Charité-Universitätsmedizin Berlin, corporate member of Freie

11 Universität Berlin, Humboldt-Universität zu Berlin, and Berlin Institute of Health, Berlin,

12 Germany.

13 [5] Fogarty International Center, National Institutes of Health, Bethesda, Maryland, USA.

14 [6] Martsinovsky Institute of Medical Parasitology, Tropical and Vector Borne Diseases, Sechenov

15 University, Moscow, Russia.

16 [7] Emerging Infectious Diseases Program, Duke-National University of Singapore Medical

17 School, Singapore.

18 [8] Royal Netherlands Institute for Sea Research, Department of Coastal Systems, and Utrecht

19 University, the Netherlands

20

21

22

23

Abstract

Bats host virulent zoonotic viruses without experiencing disease. A mechanistic understanding of the impact of bats' virus hosting capacities, including uniquely constitutive immune pathways, on cellular-scale viral dynamics is needed to elucidate zoonotic emergence. We carried out virus infectivity assays on bat cell lines expressing induced and constitutive immune phenotypes, then developed a theoretical model of our *in vitro* system, which we fit to empirical data. Best fit models recapitulated expected immune phenotypes for representative cell lines, supporting robust antiviral defenses in bat cells that correlated with higher estimates for within-host viral propagation rates. In general, heightened immune responses limit pathogen-induced cellular morbidity, which can facilitate the establishment of rapidly-propagating persistent infections within-host. Rapidly-replicating viruses that have evolved with bat immune systems will likely cause enhanced virulence following emergence into secondary hosts with immune systems that diverge from those unique to bats.

47 **Introduction**

48 Bats have received much attention in recent years for their role as reservoir hosts for
49 emerging viral zoonoses, including rabies and related lyssaviruses, Hendra and Nipah
50 henipaviruses, Ebola and Marburg filoviruses, and SARS coronavirus (Calisher et al. 2006;
51 Wang and Anderson 2019). In most non-Chiropteran mammals, henipaviruses, filoviruses, and
52 coronaviruses induce substantial morbidity and mortality, display short durations of infection,
53 and elicit robust, long-term immunity in hosts surviving infection (Nicholls et al. 2003; Hooper
54 et al. 2001; Mahanty and Bray 2004). Bats, by contrast, demonstrate no obvious disease
55 symptoms upon infection with pathogens that are highly virulent in non-volant mammals
56 (Schountz et al. 2017) but may, instead, support viruses as long-term persistent infections, rather
57 than transient, immunizing pathologies (Plowright et al. 2016).

58 Recent research advances are beginning to shed light on the molecular mechanisms by
59 which bats avoid pathology from these otherwise virulent pathogens (Brook and Dobson 2015).
60 Bats leverage a suite of species-specific mechanisms to limit viral load, which include host
61 receptor sequence incompatibilities for some bat-virus combinations (Ng et al. 2015; Igarashi et
62 al. 2020) and constitutive expression of the antiviral cytokine, IFN-α, for others (Zhou et al.
63 2016). Typically, the presence of viral RNA or DNA in the cytoplasm of mammalian cells will
64 induce secretion of type I interferon proteins (IFN-α and IFN-β), which promote expression and
65 translation of interferon-stimulated genes (ISGs) in neighboring cells and render them effectively
66 antiviral (Stetson and Medzhitov 2006). In some bat cells, the transcriptomic blueprints for this
67 IFN response are expressed constitutively, even in the absence of stimulation by viral RNA or
68 DNA (Zhou et al. 2016). In non-flying mammals, constitutive IFN expression would likely elicit
69 widespread inflammation and concomitant immunopathology upon viral infection, but bats

70 support unique adaptations to combat inflammation (Zhang et al. 2013; Ahn et al. 2019; Xie et
71 al. 2018; Pavlovich et al. 2018) that may have evolved to mitigate metabolic damage induced
72 during flight (Kacprzyk et al. 2017). The extent to which constitutive IFN-α expression signifies
73 constitutive antiviral defense in the form of functional IFN-α protein remains unresolved. In bat
74 cells constitutively expressing IFN-α, some protein-stimulated, downstream ISGs appear to be
75 also constitutively expressed, but additional ISG induction is nonetheless possible following viral
76 challenge and stimulation of IFN-β (Zhou et al. 2016; Xie et al. 2018). Despite recent advances
77 in molecular understanding of bat viral tolerance, the consequences of this unique bat immunity
78 on within-host virus dynamics—and its implications for understanding zoonotic emergence—
79 have yet to be elucidated.

80 The field of 'virus dynamics' was first developed to describe the mechanistic
81 underpinnings of long-term patterns of steady-state viral load exhibited by patients in chronic
82 phase infections with HIV, who appeared to produce and clear virus at equivalent rates (Nowak
83 and May 2000; Ho et al. 1995). Models of simple target cell depletion, in which viral load is
84 dictated by a bottom-up resource supply of infection-susceptible host cells, were first developed
85 for HIV (Perelson 2002) but have since been applied to other chronic infections, including
86 hepatitis-C virus (Neumann et al. 1998), hepatitis-B virus (Nowak et al. 1996) and
87 cytomegalovirus (Emery et al. 1999). Recent work has adopted similar techniques to model the
88 within-host dynamics of acute infections, such as influenza A and measles, inspiring debate over
89 the extent to which explicit modeling of top-down immune control can improve inference
90 beyond the basic resource limitation assumptions of the target cell model (Baccam et al. 2006;
91 Pawelek et al. 2012; Saenz et al. 2010; Morris et al. 2018).

92 To investigate the impact of unique bat immune processes on *in vitro* viral kinetics, we
93 first undertook a series of virus infection experiments on bat cell lines expressing divergent
94 interferon phenotypes, then developed a theoretical model elucidating the dynamics of within-
95 host viral spread. We evaluated our theoretical model analytically independent of the data, then
96 fit the model to data recovered from *in vitro* experimental trials in order to estimate rates of
97 within-host virus transmission and cellular progression to antiviral status under diverse
98 assumptions of absent, induced, and constitutive immunity. Finally, we confirmed our findings in
99 spatially-explicit stochastic simulations of fitted time series from our mean field model. We
100 hypothesized that top-down immune processes would overrule classical resource-limitation in
101 bat cell lines described as constitutively antiviral in the literature, offering a testable prediction
102 for models fit to empirical data. We further predicted that the most robust antiviral responses
103 would be associated with the most rapid within-host virus propagation rates but also protect cells
104 against virus-induced mortality to support the longest enduring infections in tissue culture.
105

106 **Results**

107 **Virus infection experiments in antiviral bat cell cultures yield reduced cell mortality and**
108 **elongated epidemics.**

109 We first explored the influence of innate immune phenotype on within-host viral
110 propagation in a series of infection experiments in cell culture. We conducted plaque assays on
111 six-well plate monolayers of three immortalized mammalian kidney cell lines: [1] Vero (African
112 green monkey) cells, which are IFN-defective and thus limited in antiviral capacity (Desmyter,
113 Melnick, and Rawls 1968); [2] RoNi/7.1 (*Rousettus aegyptiacus*) cells which demonstrate
114 idiosyncratic induced interferon responses upon viral challenge (Kuzmin et al. 2017; Arnold et

115 al. 2018; Biesold et al. 2011; Pavlovich et al. 2018); and [3] PaKiT01 (*Pteropus alecto*) cells
116 which constitutively express IFN-α (Zhou et al. 2016; Crameri et al. 2009). To intensify cell
117 line-specific differences in constitutive immunity, we carried out infectivity assays with GFP-
118 tagged, replication-competent vesicular stomatitis Indiana viruses: rVSV-G, rVSV-EBOV, and
119 rVSV-MARV, which have been previously described (Miller et al. 2012; Wong et al. 2010).
120 Two of these viruses, rVSV-EBOV and rVSV-MARV, are recombinants for which cell entry is
121 mediated by the glycoprotein of the bat-evolved filoviruses, Ebola (EBOV) and Marburg
122 (MARV), thus allowing us to modulate the extent of structural, as well as immunological,
123 antiviral defense at play in each infection. Previous work in this lab has demonstrated
124 incompatibilities in the NPC1 filovirus receptor which render PaKiT01 cells refractory to
125 infection with rVSV-MARV (Ng and Chandran 2018), making them structurally antiviral, over
126 and above their constitutive expression of IFN-α. All three cell lines were challenged with all
127 three viruses at two multiplicities of infection (MOI): 0.001 and 0.0001. Between 18-39 trials
128 were run at each cell-virus-MOI combination, excepting rVSV-MARV infections on PaKiT01
129 cells at MOI=0.001, for which only 8 trials were run (see Materials and Methods; Figure 1-figure
130 supplement 1-3, Supplementary File 1).
131 Because plaque assays restrict viral transmission neighbor-to-neighbor in two-
132 dimensional cellular space (Howat et al. 2006), we were able to track the spread of GFP-
133 expressing virus-infected cells across tissue monolayers via inverted fluorescence microscopy.
134 For each infection trial, we monitored and re-imaged plates for up to 200 hours of observations
135 or until total monolayer destruction, processed resulting images, and generated a time series of
136 the proportion of infectious-cell occupied plate space across the duration of each trial (see
137 Materials and Methods). We used generalized additive models to infer the time course of all cell

138 culture replicates and construct the multi-trial dataset to which we eventually fit our mechanistic
139 transmission model for each cell line-virus-specific combination (Figure 1; Figure 1-figure
140 supplement 1-5).

141 All three recombinant vesicular stomatitis viruses (rVSV-G, rVSV-EBOV, and rVSV-
142 MARV) infected Vero, RoNi/7.1, and PaKiT01 tissue cultures at both focal MOIs. Post-
143 invasion, virus spread rapidly across most cell monolayers, resulting in virus-induced epidemic
144 extinction. Epidemics were less severe in bat cell cultures, especially when infected with the
145 recombinant filoviruses, rVSV-EBOV and rVSV-MARV. Monolayer destruction was avoided in
146 the case of rVSV-EBOV and rVSV-MARV infections on PaKiT01 cells: in the former, persistent
147 viral infection was maintained throughout the 200-hour duration of each experiment, while, in
148 the latter, infection was eliminated early in the time series, preserving a large proportion of live,
149 uninfectious cells across the duration of the experiment. We assumed this pattern to be the result
150 of immune-mediated epidemic extinction (Figure 1). Patterns from MOI=0.001 were largely
151 recapitulated at MOI = 0.0001, though at somewhat reduced total proportions (Figure 1-figure
152 supplement 5).

153

154 **A theoretical model fit to *in vitro* data recapitulates expected immune phenotypes for bat**
155 **cells.**

156 We next developed a within-host model to fit to these data in order to elucidate the
157 effects of induced and constitutive immunity on the dynamics of viral spread in host tissue
158 (Figure 1). The compartmental within-host system mimicked our two-dimensional cell culture
159 monolayer, with cells occupying five distinct infection states: susceptible (S), antiviral (A),
160 exposed (E), infectious (I), and dead (D). We modeled exposed cells as infected but not yet

161 infectious, capturing the 'eclipse phase' of viral integration into a host cell which precedes viral
162 replication. Antiviral cells were immune to viral infection, in accordance with the "antiviral
163 state" induced from interferon stimulation of ISGs in tissues adjacent to infection (Stetson and
164 Medzhitov 2006). Because we aimed to translate available data into modeled processes, we did
165 not explicitly model interferon dynamics but instead scaled the rate of cell progression from
166 susceptible to antiviral (ρ) by the proportion of exposed cells (globally) in the system. In systems
167 permitting constitutive immunity, a second rate of cellular acquisition of antiviral status (ε)
168 additionally scaled with the global proportion of susceptible cells in the model. Compared with
169 virus, IFN particles are small and highly diffusive, justifying this global signaling assumption at
170 the limited spatial extent of a six well plate and maintaining consistency with previous modeling
171 approximations of IFN signaling in plaque assay (Howat et al. 2006).

172 To best represent our empirical monolayer system, we expressed our state variables as
173 proportions (P_s, P_A, P_E, P_I, and P_D), under assumptions of frequency-dependent transmission in a
174 well-mixed population (Keeling and Rohani 2008), though note that the inclusion of P_D
175 (representing the proportion of dead space in the modeled tissue) had the functional effect of
176 varying transmission with infectious cell density. This resulted in the following system of
177 ordinary differential equations:

178

179 $$\frac{dP_s}{dt} = bP_D(P_s + P_A) - \beta P_S P_I - \mu P_s - \rho P_E P_s - \varepsilon P_s + cP_A \quad (1)$$

180 $$\frac{dP_A}{dt} = \rho P_E P_s + \varepsilon P_s - cP_A - \mu P_A \quad (2)$$

181 $$\frac{dP_E}{dt} = \beta P_S P_I - \sigma P_E - \mu P_E \quad (3)$$

182 $$\frac{dP_I}{dt} = \sigma P_E - \alpha P_I - \mu P_I \quad (4)$$

183 $$\frac{dP_D}{dt} = \mu(P_s + P_E + P_I + P_A) + \alpha P_I - bP_D(P_s + P_A) \quad (5)$$

184

185 We defined "induced immunity" as complete, modeling all cells as susceptible to viral
186 invasion at disease free equilibrium, with defenses induced subsequent to viral exposure through
187 the term ρ. By contrast, we allowed the extent of constitutive immunity to vary across the
188 parameter range of $\varepsilon > 0$, defining a "constitutive" system as one containing *any* antiviral cells at
189 disease free equilibrium. In fitting this model to tissue culture data, we independently estimated
190 both ρ and ε, as well as the cell-to-cell transmission rate, β, for each cell-virus combination.
191 Since the extent to which constitutively-expressed IFN-α is constitutively translated into
192 functional protein is not yet known for bat hosts (Zhou et al. 2016), this approach permitted our
193 tissue culture data to drive modeling inference: even in PaKiT01 cell lines known to
194 constitutively express IFN-α, the true constitutive extent of the system (i.e. the quantity of
195 antiviral cells present at disease free equilibrium) was allowed to vary through estimation of ε.
196 For the purposes of model-fitting, we fixed the value of c, the return rate of antiviral cells to
197 susceptible status, at 0. The small spatial scale and short time course (max 200 hours) of our
198 experiments likely prohibited any return of antiviral cells to susceptible status in our empirical
199 system; nonetheless, we retained the term c in analytical evaluations of our model because
200 regression from antiviral to susceptible status is possible over long time periods *in vitro* and at
201 the scale of a complete organism (Samuel and Knutson 1982; Rasmussen and Farley 1975;
202 Radke et al. 1974).

203 Before fitting to empirical time series, we undertook bifurcation analysis of our
204 theoretical model and generated testable hypotheses on the basis of model outcomes. From our

205 within-host model system (equations 1-5), we derived the following expression for R_0, the

206 pathogen basic reproduction number (Supplementary File 2):

207 $$R_0 = \frac{\beta\sigma(b-\mu)(c+\mu)}{b(\sigma+\mu)(\alpha+\mu)(c+\mu+\varepsilon)} \quad (6)$$

208 Pathogens can invade a host tissue culture when $R_0 > 1$. Rapid rates of constitutive antiviral

209 acquisition (ε) will drive $R_0 < 1$: tissue cultures with highly constitutive antiviral immunity will

210 be therefore resistant to virus invasion from the outset. Since, by definition, induced immunity is

211 stimulated following initial virus invasion, the rate of induced antiviral acquisition (ρ) is not

212 incorporated into the equation for R_0; while induced immune processes can control virus after

213 initial invasion, they cannot prevent it from occurring to begin with. In cases of fully induced or

214 absent immunity ($\varepsilon = 0$), the R_0 equation thus reduces to a form typical of the classic SEIR

215 model:

216 $$R_0 = \frac{\beta\sigma(b-\mu)}{b(\alpha+\mu)(\sigma+\mu)} \quad (7)$$

217 At equilibrium, the theoretical, mean field model demonstrates one of three infection

218 states: endemic equilibrium, stable limit cycles, or no infection (Figure 2). Respectively, these

219 states approximate the persistent infection, virus-induced epidemic extinction, and immune-

220 mediated epidemic extinction phenotypes previously witnessed in tissue culture experiments

221 (Figure 1). Theoretically, endemic equilibrium is maintained when new infections are generated

222 at the same rate at which infections are lost, while limit cycles represent parameter space under

223 which infectious and susceptible populations are locked in predictable oscillations. Endemic

224 equilibria resulting from cellular regeneration (i.e. births) have been described *in vivo* for HIV

225 (Coffin 1995) and *in vitro* for herpesvirus plaque assays (Howat et al. 2006), but, because they so

226 closely approach zero, true limit cycles likely only occur theoretically, instead yielding stochastic

227 extinctions in empirical time series.

228 Bifurcation analysis of our mean field model revealed that regions of no infection
229 (pathogen extinction) were bounded at lower threshold (Branch point) values for β, below which
230 the pathogen was unable to invade. We found no upper threshold to invasion for β under any
231 circumstances (i.e. β high enough to drive pathogen-induced extinction), but high β values
232 resulted in Hopf bifurcations, which delineate regions of parameter space characterized by limit
233 cycles. Since limit cycles so closely approach zero, high βs recovered in this range would likely
234 produce virus-induced epidemic extinctions under experimental conditions. Under more robust
235 representations of immunity, with higher values for either or both induced (ρ) and constitutive
236 (ε) rates of antiviral acquisition, Hopf bifurcations occurred at increasingly higher values for β,
237 meaning that persistent infections could establish at higher viral replication rates (Figure 2).
238 Consistent with our derivation for R_0, we found that the Branch point threshold for viral invasion
239 was independent of changes to the induced immune parameter (ρ) but saturated at high values of
240 ε that characterize highly constitutive immunity (Figure 3).
241 We next fit our theoretical model by least squares to each cell line-virus combination,
242 under absent, induced, and constitutive assumptions of immunity. In general, best fit models
243 recapitulated expected outcomes based on the immune phenotype of the cell line in question, as
244 described in the general literature (Table 1; Supplementary File 4). The absent immune model
245 offered the most accurate approximation of IFN-deficient Vero cell time series, the induced
246 immune model best recovered the RoNi/7.1 cell trials, and, in most cases, the constitutive
247 immune model most closely recaptured infection dynamics across constitutively IFN-α-
248 expressing PaKiT01 cell lines (Figure 1; Figure 1-figure supplement 4-5, Supplementary File 4).
249 Ironically, the induced immune model offered a slightly better fit than the constitutive to rVSV-
250 MARV infections on the PaKiT01 cell line (the one cell line-virus combination for which we

251 know a constitutively antiviral cell-receptor incompatibility to be at play). Because constitutive
252 immune assumptions can prohibit pathogen invasion ($R_0 < 1$), model fits to this time series
253 under constitutive assumptions were handicapped by overestimations of ε, which prohibited
254 pathogen invasion. Only by incorporating an exceedingly rapid rate of induced antiviral
255 acquisition could the model guarantee that initial infection would be permitted and then rapidly
256 controlled.
257
258 **Robust immunity is linked to rapid within-host virus transmission rates in fitted models.**
259 In fitting our theoretical model to *in vitro* data, we estimated the within-host virus
260 transmission rate (β) and the rate(s) of cellular acquisition to antiviral status (ρ or ρ + ε) (Table
261 1; Supplementary File 4). Under absent immune assumptions, ρ and ε were fixed at 0 while β
262 was estimated; under induced immune assumptions, ε was fixed at 0 while ρ and β were
263 estimated; and under constitutive immune assumptions, all three parameters (ρ, ε, and β) were
264 simultaneously estimated for each cell-virus combination. Best fit parameter estimates for
265 MOI=0.001 data are visualized in conjunction with β – ρ and β – ε bifurcations in Figure 4; all
266 general patterns were recapitulated at lower values for β on MOI=0.0001 trials (Figure 4-figure
267 supplement 1).
268 As anticipated, the immune absent model (a simple target cell model) offered the best fit
269 to IFN-deficient Vero cell infections (Figure 4; Table 1; Supplementary File 4). Among Vero
270 cell trials, infections with rVSV-G produced the highest β estimates, followed by infections with
271 rVSV-EBOV and rVSV-MARV. Best fit parameter estimates on Vero cell lines localized in the
272 region of parameter space corresponding to theoretical limit cycles, consistent with observed
273 virus-induced epidemic extinctions in stochastic tissue cultures.

274 In contrast to Vero cells, the induced immunity model offered the best fit to all RoNi/7.1
275 data, consistent with reported patterns in the literature and our own validation by qPCR (Table 1;
276 Figure 1-figure supplement 6; Biesold et al. 2011; Kuzmin et al. 2017; Arnold et al. 2018;
277 Pavlovich et al. 2018). As in Vero cell trials, we estimated highest β values for rVSV-G
278 infections on RoNi/7.1 cell lines but here recovered higher β estimates for rVSV-MARV than for
279 rVSV-EBOV. This reversal was balanced by a higher estimated rate of acquisition to antiviral
280 status (ρ) for rVSV-EBOV versus rVSV-MARV. In general, we observed that more rapid rates
281 of antiviral acquisition (either induced, ρ, constitutive, ε, or both) correlated with higher
282 transmission rates (β). When offset by ρ, β values estimated for RoNi/7.1 infections maintained
283 the same amplitude as those estimated for immune-absent Vero cell lines but caused gentler
284 epidemics and reduced cellular mortality (Figure 1). RoNi/7.1 parameter estimates localized in
285 the region corresponding to endemic equilibrium for the deterministic, theoretical model (Figure
286 4), yielding less acute epidemics which nonetheless went extinct in stochastic experiments.
287 Finally, rVSV-G and rVSV-EBOV trials on PaKiT01 cells were best fit by models
288 assuming constitutive immunity, while rVSV-MARV infections on PaKiT01 were matched
289 equivalently by models assuming either induced or constitutive immunity—with induced models
290 favored over constitutive in AIC comparisons because one fewer parameter was estimated
291 (Figure 1-figure supplement 4-5; Supplementary File 4). For all virus infections, PaKiT01 cell
292 lines yielded β estimates a full order of magnitude higher than Vero or RoNi/7.1 cells, with each
293 β balanced by an immune response (either ρ, or ρ combined with ε) also an order of magnitude
294 higher than that recovered for the other cell lines (Figure 4; Table 1). As in RoNi/7.1 cells,
295 PaKiT01 parameter fits localized in the region corresponding to endemic equilibrium for the
296 deterministic theoretical model. Because constitutive immune processes can actually prohibit

297 initial pathogen invasion, constitutive immune fits to rVSV-MARV infections on PaKiT01 cell
298 lines consistently localized at or below the Branch point threshold for virus invasion ($R_0 = 1$).
299 During model fitting for optimization of ε, any parameter tests of ε values producing $R_0 < 1$
300 resulted in no infection and, consequently, produced an exceedingly poor fit to infectious time
301 series data. In all model fits assuming constitutive immunity, across all cell lines, parameter
302 estimates for ρ and ε traded off, with one parameter optimized at values approximating zero,
303 such that the immune response was modeled as almost entirely induced or entirely constitutive
304 (Table 1; Supplementary File 4). For RoNi/7.1 cells, even when constitutive immunity was
305 allowed, the immune response was estimated as almost entirely induced, while for rVSV-G and
306 rVSV-EBOV fits on PaKiT01 cells, the immune response optimized as almost entirely
307 constitutive. For rVSV-MARV on PaKiT01 cells, however, estimation of ρ was high under all
308 assumptions, such that any additional antiviral contributions from ε prohibited virus from
309 invading at all. The induced immune model thus produced a more parsimonious recapitulation of
310 these data because virus invasion was always permitted, then rapidly controlled.
311

312 **Antiviral cells safeguard live cells against rapid cell mortality to elongate epidemic**
313 **duration *in vitro*.**

314 In order to compare the relative contributions of each cell line's disparate immune
315 processes to epidemic dynamics, we next used our mean field parameter estimates to calculate
316 the initial 'antiviral rate'—the initial accumulation rate of antiviral cells upon virus invasion for
317 each cell-virus-MOI combination—based on the following equation:

318 $$Antiviral\ Rate = \rho P_E P_s - \varepsilon P_s \quad (8)$$

319 where P_E was calculated from the initial infectious dose (MOI) of each infection experiment and

320 P_S was estimated at disease free equilibrium:

321 $$P_E = 1 - e^{-MOI} \quad (9)$$

322 $$P_S = \frac{(b-\mu)(c+\mu)}{b(c+\mu+\varepsilon)} \quad (10)$$

323 Because ρ and ε both contribute to this initial antiviral rate, induced and constitutive immune

324 assumptions are capable of yielding equally rapid rates, depending on parameter fits. Indeed,

325 under fully induced immune assumptions, the induced antiviral acquisition rate (ρ) estimated for

326 rVSV-MARV infection on PaKiT01 cells was so high that the initial antiviral rate exceeded even

327 that estimated under constitutive assumptions for this cell-virus combination (Supplementary

328 File 4). In reality, we know that NPC1 receptor incompatibilities make PaKiT01 cell lines

329 constitutively refractory to rVSV-MARV infection (Ng and Chandran 2018) and that PaKiT01

330 cells also constitutively express the antiviral cytokine, IFN-α. Model fitting results suggest that

331 this constitutive expression of IFN-α may act more as a rapidly inducible immune response

332 following virus invasion than as a constitutive secretion of functional IFN-α protein.

333 Nonetheless, as hypothesized, PaKiT01 cell lines were by far the most antiviral of any in our

334 study—with initial antiviral rates estimated several orders of magnitude higher than any others in

335 our study, under either induced or constitutive assumptions (Table 1; Supplementary File 4).

336 RoNi/7.1 cells displayed the second-most-pronounced signature of immunity, followed by Vero

337 cells, for which the initial antiviral rate was essentially zero even under forced assumptions of

338 induced or constitutive immunity (Table 1; Supplementary File 4).

339 Using fitted parameters for β and ε, we additionally calculated R_0, the basic reproduction

340 number for the virus, for each cell line-virus-MOI combination (Table 1; Supplementary File 4).

341 We found that R_0 was essentially unchanged across differing immune assumptions for RoNi/7.1

342 and Vero cells, for which the initial antiviral rate was low. In the case of PaKiT01 cells, a high
343 initial antiviral rate under either induced or constitutive immunity resulted in a correspondingly
344 high estimation of β (and, consequently, R_0) which still produced the same epidemic curve that
345 resulted from the much lower estimates for β and R_0 paired with absent immunity. These
346 findings suggest that antiviral immune responses protect host tissues against virus-induced cell
347 mortality and may facilitate the establishment of more rapid within-host transmission rates.
348 Total monolayer destruction occurred in all cell-virus combinations excepting rVSV-
349 EBOV infections on RoNi/7.1 cells and rVSV-EBOV and rVSV-MARV infections on PaKiT01
350 cells. Monolayer destruction corresponded to susceptible cell depletion and epidemic turnover
351 where R-effective (the product of R_0 and the proportion susceptible) was reduced below one
352 (Figure 5). For rVSV-EBOV infections on RoNi/7.1, induced antiviral cells safeguarded remnant
353 live cells, which birthed new susceptible cells late in the time series. In rVSV-EBOV and rVSV-
354 MARV infections on PaKiT01 cells, this antiviral protection halted the epidemic (Figure 5; R-
355 effective <1) before susceptibles fully declined. In the case of rVSV-EBOV on PaKiT01, the
356 birth of new susceptibles from remnant live cells protected by antiviral status maintained late-
357 stage transmission to facilitate long-term epidemic persistence. Importantly, under fixed
358 parameter values for the infection incubation rate (σ) and infection-induced mortality rate (α),
359 models were unable to reproduce the longer-term infectious time series captured in data from
360 rVSV-EBOV infections on PaKiT01 cell lines without incorporation of cell births, an
361 assumption adopted in previous modeling representations of IFN-mediated viral dynamics in
362 tissue culture (Howat et al. 2006). In our experiments, we observed that cellular reproduction
363 took place as plaque assays achieved confluency.

364 Finally, because the protective effect of antiviral cells is more clearly observable
365 spatially, we confirmed our results by simulating fitted time series in a spatially-explicit,
366 stochastic reconstruction of our mean field model. In spatial simulations, rates of antiviral
367 acquisition were fixed at fitted values for ρ and ε derived from mean field estimates, while
368 transmission rates (β) were fixed at values ten times greater than those estimated under mean
369 field conditions, accounting for the intensification of parameter thresholds permitting pathogen
370 invasion in local spatial interactions (see Materials and Methods; Videos 1-3; Figure 5-figure
371 supplement 3; Supplementary File 5; Webb, Keeling, and Boots 2007). In immune capable time
372 series, spatial antiviral cells acted as 'refugia' which protected live cells from infection as each
373 initial epidemic wave 'washed' across a cell monolayer. Eventual birth of new susceptibles from
374 these living refugia allowed for sustained epidemic transmission in cases where some infectious
375 cells persisted at later timepoints in simulation (Videos 1-3; Figure 5- figure supplement 3).
376

377 **Discussion**

378 Bats are reservoirs for several important emerging zoonoses but appear not to experience
379 disease from otherwise virulent viral pathogens. Though the molecular biological literature has
380 made great progress in elucidating the mechanisms by which bats tolerate viral infections (Zhou
381 et al. 2016; Ahn et al. 2019; Xie et al. 2018; Pavlovich et al. 2018; Zhang et al. 2013), the impact
382 of unique bat immunity on virus dynamics within-host has not been well-elucidated. We used an
383 innovative combination of *in vitro* experimentation and within-host modeling to explore the
384 impact of unique bat immunity on virus dynamics. Critically, we found that bat cell lines
385 demonstrated a signature of enhanced interferon-mediated immune response, of either
386 constitutive or induced form, which allowed for establishment of rapid within-host, cell-to-cell

virus transmission rates (β). These results were supported by both data-independent bifurcation analysis of our mean field theoretical model, as well as fitting of this model to viral infection time series established in bat cell culture. Additionally, we demonstrated that the antiviral state induced by the interferon pathway protects live cells from mortality in tissue culture, resulting in *in vitro* epidemics of extended duration that enhance that probability of establishing a long-term persistent infection. Our findings suggest that viruses evolved in bat reservoirs possessing enhanced IFN capabilities could achieve more rapid within-host transmission rates without causing pathology to their hosts. Such rapidly-reproducing viruses would likely generate extreme virulence upon spillover to hosts lacking similar immune capacities to bats.

To achieve these results, we first developed a novel, within-host, theoretical model elucidating the effects of unique bat immunity, then undertook bifurcation analysis of the model's equilibrium properties under immune absent, induced, and constitutive assumptions. We considered a cell line to be constitutively immune if possessing any number of antiviral cells at disease free equilibrium but allowed the extent of constitutive immunity to vary across the parameter range for ε, the constitutive rate of antiviral acquisition. In deriving the equation for R_0, the basic reproduction number, which defines threshold conditions for virus invasion of a tissue ($R_0 > 1$), we demonstrated how the invasion threshold is elevated at high values of constitutive antiviral acquisition, ε. Constitutive immune processes can thus prohibit pathogen invasion, while induced responses, by definition, can only control infections *post-hoc*. Once thresholds for pathogen invasion have been met, assumptions of constitutive immunity will limit the cellular mortality (virulence) incurred at high transmission rates. Regardless of mechanism (induced or constitutive), interferon-stimulated antiviral cells appear to play a key role in

409 maintaining longer term or persistent infections by safeguarding susceptible cells from rapid
410 infection and concomitant cell death.

411 Fitting of our model to *in vitro* data supported expected immune phenotypes for different
412 bat cell lines as described in the literature. Simple target cell models that ignore the effects of
413 immunity best recapitulated infectious time series derived from IFN-deficient Vero cells, while
414 models assuming induced immune processes most accurately reproduced trials derived from
415 RoNi/7.1 (*Rousettus aegyptiacus*) cells, which possesses a standard virus-induced IFN-response.
416 In most cases, models assuming constitutive immune processes best recreated virus epidemics
417 produced on PaKiT01 (*Pteropus alecto*) cells, which are known to constitutively express the
418 antiviral cytokine, IFN-α (Zhou et al. 2016). Model support for induced immune assumptions in
419 fits to rVSV-MARV infections on PaKiT01cells suggests that the constitutive IFN-α expression
420 characteristic of *P. alecto* cells may represent more of a constitutive immune priming process
421 than a perpetual, functional, antiviral defense. Results from mean field model fitting were
422 additionally confirmed in spatially explicit stochastic simulations of each time series.

423 As previously demonstrated in within-host models for HIV (Coffin 1995; Perelson et al.
424 1996; Nowak et al. 1995; Bonhoeffer et al. 1997; Ho et al. 1995), assumptions of simple target-
425 cell depletion can often provide satisfactory approximations of viral dynamics, especially those
426 reproduced in simple *in vitro* systems. Critically, our model fitting emphasizes the need for
427 incorporation of top-down effects of immune control in order to accurately reproduce infectious
428 time series derived from bat cell tissue cultures, especially those resulting from the robustly
429 antiviral PaKiT01 *P. alecto* cell line. These findings indicate that enhanced IFN-mediated
430 immune pathways in bat reservoirs may promote elevated within-host virus replication rates
431 prior to cross-species emergence. We nonetheless acknowledge the limitations imposed by *in*

432 *vitro* experiments in tissue culture, especially involving recombinant viruses and immortalized
433 cell lines. Future work should extend these cell culture studies to include measurements of
434 multiple state variables (i.e. antiviral cells) to enhance epidemiological inference.
435 The continued recurrence of Ebola epidemics across central Africa highlights the
436 importance of understanding bats' roles as reservoirs for virulent zoonotic disease. The past
437 decade has born witness to emerging consensus regarding the unique pathways by which bats
438 resist and tolerate highly virulent infections (Brook and Dobson 2015; Xie et al. 2018; Zhang et
439 al. 2013; Ahn et al. 2019; Zhou et al. 2016; Ng et al. 2015; Pavlovich et al. 2018). Nonetheless,
440 an understanding of the mechanisms by which bats support endemic pathogens at the population
441 level, or promote the evolution of virulent pathogens at the individual level, remains elusive.
442 Endemic maintenance of infection is a defining characteristic of a pathogen reservoir (Haydon et
443 al. 2002), and bats appear to merit such a title, supporting long-term persistence of highly
444 transmissible viral infections in isolated island populations well below expected critical
445 community sizes (Peel et al. 2012). Researchers debate the relative influence of population-level
446 and within-host mechanisms which might explain these trends (Plowright et al. 2016), but
447 increasingly, field data are difficult to reconcile without acknowledgement of a role for persistent
448 infections (Peel et al. 2018; Brook et al. 2019). We present general methods to study cross-scale
449 viral dynamics, which suggest that within-host persistence is supported by robust antiviral
450 responses characteristic of bat immune processes. Viruses which evolve rapid replication rates
451 under these robust antiviral defenses may pose the greatest hazard for cross-species pathogen
452 emergence into spillover hosts with immune systems that differ from those unique to bats.
453
454

455 **Materials and Methods**

456

Key Resources Table*				
Reagent type (species) or resource	**Designation**	**Source or reference**	**Identifiers**	**Additional information**
cell line (Vero)	Kidney (normal, epithelial, adult)	ATCC	CCL-81	
cell line (*Rousettus aegyptiacus)*	Kidney (normal, epithelial, adult)	(Biesold et al. 2011; Kühl et al. 2011)	RoNi/7.1	
cell line (*Pteropus alecto*)	Kidney (normal, epithelial, adult)	(Crameri et al. 2009)	PaKiT01	
virus strain	Replication competent, recombinant vesicular stomatitis Indiana virus expressing eGFP	(Miller et al. 2012; Wong et al. 2010)	rVSV-G	
virus strain	Replication competent, recombinant vesicular stomatitis Indiana virus expressing eGFP & EBOV GP in place of VSV G	(Miller et al. 2012; Wong et al. 2010)	rVSV-EBOV	
virus strain	Replication competent, recombinant vesicular stomatitis Indiana virus expressing eGFP & MARV GP in place of VSV G	(Miller et al. 2012; Wong et al. 2010)	rVSV-MARV	
reagent	Hoechst 33342 Fluorescent Stain	ThermoFisher	cat #: 62249	
reagent	L-Glutamine Solution	ThermoFisher	cat #: 25030081	
reagent	Gibco HEPES	ThermoFisher	cat #: 15630080	

reagent	iTaq Universal SYBR Green Supermix	BioRad	cat #: 1725120	
commercial assay or kit	Quick RNA Mini Prep Kit	Zymo	cat #: R1054	
commercial assay or kit	Invitrogen Superscript III cDNA Synthesis Kit	ThermoFisher	cat #: 18080051	
software	MatCont (version 2.2)	(Dhooge et al. 2008)	MatCont	
R	R version 3.6.0	(R Core Team 2019)	R	
*Note that primers for *R. aegyptiacus* and *P. alecto* β-Actin, IFN-α, and IFN-β genes are listed in the Supplementary File 6.				

457

458 **Cell Culture Experiments.**

459 *Cells*.

460 All experiments were carried out on three immortalized mammalian kidney cell lines:
461 Vero (African green monkey), RoNi/7.1 (*Rousettus aegyptiacus*) (Kühl et al. 2011; Biesold et al.
462 2011) and PaKiT01 (*Pteropus alecto*) (Crameri et al. 2009). The species identification of all bat
463 cell lines were confirmed morphologically and genetically in the publications in which they were
464 originally described (Kühl et al. 2011; Biesold et al. 2011; Crameri et al. 2009). Vero cells were
465 obtained from ATCC.

466 Monolayers of each cell line were grown to 90% confluency (~9 x 10^5 cells) in 6-well
467 plates. Cells were maintained in a humidified 37˚C, 5% CO_2 incubator and cultured in
468 Dulbecco's modified Eagle medium (DMEM) (Life Technologies, Grand Island, NY),
469 supplemented with 2% fetal bovine serum (FBS) (Gemini Bio Products, West Sacramento, CA),
470 and 1% penicillin-streptomycin (Life Technologies). Cells were tested monthly for mycoplasma

471 contamination while experiments were taking place; all cells assayed negative for contamination
472 at every testing.
473 Previous work has demonstrated that all cell lines used are capable of mounting a type I
474 IFN response upon viral challenge, with the exception of Vero cells, which possess an IFN-β
475 deficiency (Desmyter, Melnick, and Rawls 1968; Rhim et al. 1969; Emeny and Morgan 1979).
476 RoNi/7.1 cells have been shown to mount idiosyncratic induced IFN defenses upon viral
477 infection (Pavlovich et al. 2018; Kuzmin et al. 2017; Arnold et al. 2018; Kühl et al. 2011;
478 Biesold et al. 2011), while PaKiT01 cells are known to constitutively express the antiviral
479 cytokine, IFN-α (Zhou et al. 2016). This work is the first documentation of IFN signaling
480 induced upon challenge with the particular recombinant VSVs outlined below. We verified
481 known antiviral immune phenotypes via qPCR. Results were consistent with the literature,
482 indicating a less pronounced role for interferon defense against viral infection in RoNi/7.1 versus
483 PaKiT01 cells.
484
485 *Viruses*.
486 Replication-capable recombinant vesicular stomatitis Indiana viruses, expressing filovirus
487 glycoproteins in place of wild type G (rVSV-G, rVSV-EBOV, and rVSV-MARV) have been
488 previously described (Wong et al. 2010; Miller et al. 2012). Viruses were selected to represent a
489 broad range of anticipated antiviral responses from host cells, based on a range of past
490 evolutionary histories between the virus glycoprotein mediating cell entry and the host cell's
491 entry receptor. These interactions ranged from the total absence of evolutionary history in the
492 case of rVSV-G infections on all cell lines to a known receptor-level cell entry incompatibility in
493 the case of rVSV-MARV infections on PaKiT01 cell lines.

494 To measure infectivities of rVSVs on each of the cell lines outlined above, so as to
495 calculate the correct viral dose for each MOI, NH_4Cl (20 mM) was added to infected cell
496 cultures at 1–2 hours post-infection to block viral spread, and individual eGFP-positive cells
497 were manually counted at 12–14 hours post-infection.
498
499 *Innate Immune Phenotypes via qPCR of IFN Genes*.
500 Previously published work indicates that immortalized kidney cell lines of *Rousettus*
501 *aegyptiacus* (RoNi/7.1) and *Pteropus alecto* (PaKiT01) exhibit different innate antiviral immune
502 phenotypes through, respectively, induced (Biesold et al. 2011; Pavlovich et al. 2018; Kühl et al.
503 2011; Arnold et al. 2018) and constitutive (Zhou et al. 2016) expression of type I interferon
504 genes. We verified these published phenotypes on our own cell lines infected with rVSV-G,
505 rVSV-EBOV, and rVSV-MARV via qPCR of IFN-α and IFN-β genes across a longitudinal time
506 series of infection.
507 Specifically, we carried out multiple time series of infection of each cell line with each of
508 the viruses described above, under mock infection conditions and at MOIs of 0.0001 and
509 0.001—with the exception of rVSV-MARV on PaKiT01 cell lines, for which infection was only
510 performed at MOI=0.0001 due to limited viral stocks and the extremely low infectivity of this
511 virus on this cell line (thus requiring high viral loads for initial infection). All experiments were
512 run in duplicate on 6-well plates, such that a typical plate for any of the three viruses had two
513 control (mock) wells, two MOI=0.0001 wells and two MOI=0.001 wells, excepting PaKiT01
514 plates, which had two control and four MOI=0.0001 wells at a given time. We justify this
515 PaKiT01 exemption through the expectation that IFN-α expression is constitutive for these cells,

516 and by the assumption that any expression exhibited at the lower MOI should also be present at
517 the higher MOI.

518 For these gene expression time series, four 6-well plates for each cell line–virus
519 combination were incubated with virus for one hour at 37˚C. Following incubation, virus was
520 aspirated off, and cell monolayers were washed in PBS, then covered with an agar plaque assay
521 overlay to mimic conditions under which infection trials were run. Plates were then harvested
522 sequentially at timepoints of roughly 5, 10, 15, and 20 hours post-infection (exact timing varied
523 as multiple trials were running simultaneously). Upon harvest of each plate, agar overlay was
524 removed, and virus was lysed and RNA extracted from cells using the Zymo Quick RNA Mini
525 Prep kit, according to the manufacturer's instructions and including the step for cellular DNA
526 digestion. Post-extraction, RNA quality was verified via nanodrop, and RNA was converted to
527 cDNA using the Invitrogen Superscript III cDNA synthesis kit, according to the manufacturer's
528 instructions. cDNA was then stored at 4˚C and as a frozen stock at -20˚C to await qPCR.

529 We undertook qPCR of cDNA to assess expression of the type I interferon genes, IFN-α
530 and IFN-β, and the housekeeping gene, β-Actin, using primers previously reported in the
531 literature (Supplementary File 6). For qPCR, 2ul of each cDNA sample was incubated with 7ul
532 of deionized water, 1ul of 5UM forward/reverse primer mix and 10ul of iTaq Universal SYBR
533 Green, then cycled on a QuantStudio3 Real-Time PCR machine under the following conditions:
534 initial denaturation at 94˚C for 2 min followed by 40 cycles of: denaturation at 95˚C (5 sec),
535 annealing at 58˚C (15 sec), and extension at 72˚C (10 sec).

536 We report simple δ-Ct values for each run, with raw Ct of the target gene of interest
537 (IFN-α or IFN-β) subtracted from raw Ct of the β-Actin housekeeping gene in Figure 1-figure
538 supplement 6. Calculation of fold change upon viral infection in comparison to mock using the

539 δ-δ-Ct method (Livak and Schmittgen 2001) was inappropriate in this case, as we wished to
540 demonstrate constitutive expression of IFN-α in PaKiT01 cells, whereby data from mock cells
541 was identical to that produced from infected cells.
542
543 *Plaque Assays and Time Series Imaging*.
544 After being grown to ~90% confluency, cells were incubated with pelleted rVSVs
545 expressing eGFP (rVSV-G, rVSV-EBOV, rVSV-MARV). Cell lines were challenged with both a
546 low (0.0001) and high (0.001) multiplicity of infection (MOI) for each virus. In a cell monolayer
547 infected at a given MOI (m), the proportion of cells (P), infected by k viral particles can be
548 described by the Poisson distribution: $P(k) = \frac{e^{-m}m^k}{k!}$, such that the number of initially infected
549 cells in an experiment equals: $1 - e^{-m}$. We assumed that a ~90% confluent culture at each
550 trial's origin was comprised of ~$9x10^5$ cells and conducted all experiments at MOIs of 0.0001
551 and 0.001, meaning that we began each trial by introducing virus to, respectively, ~81 or 810
552 cells, representing the state variable 'E' in our theoretical model. Low MOIs were selected to
553 best approximate the dynamics of mean field infection and limit artifacts of spatial structuring,
554 such as premature epidemic extinction when growing plaques collide with plate walls in cell
555 culture.
556 Six well plates were prepared with each infection in duplicate or triplicate, such that a
557 control well (no virus) and 2-3 wells each at MOI 0.001 and 0.0001 were incubated
558 simultaneously on the same plate. In total, we ran between 18-39 trials at each cell-virus-MOI
559 combination, excepting r-VSV-MARV infections on PaKiT01 cells at MOI=0.001, for which we
560 ran only 8 trials due to the low infectivity of this virus on this cell line, which required high viral
561 loads for initial infection. Cells were incubated with virus for one hour at 37˚C. Following

562 incubation, virus was aspirated off, and cell monolayers were washed in PBS, then covered with
563 a molten viscous overlay (50% 2X MEM/L-glutamine; 5% FBS; 3% HEPES; 42% agarose),
564 cooled for 20 minutes, and re-incubated in their original humidified 37˚C, 5% CO_2 environment.
565 After application of the overlay, plates were monitored periodically using an inverted
566 fluorescence microscope until the first signs of GFP expression were witnessed (~6-9.5 hours
567 post-infection, depending on the cell line and virus under investigation). From that time forward,
568 a square subset of the center of each well (comprised of either 64- or 36-subframes and
569 corresponding to roughly 60 and 40% of the entire well space) was imaged periodically, using a
570 CellInsight CX5 High Content Screening (HCS) Platform with a 4X air objective
571 (ThermoFisher, Inc., Waltham, MA). Microscope settings were held standard across all trials,
572 with exposure time fixed at 0.0006 sec for each image. One color channel was imaged, such that
573 images produced show GFP-expressing cells in white and non-GFP-expressing cells in black
574 (Figure 1-figure supplement 1).
575 Wells were photographed in rotation, as frequently as possible, from the onset of GFP
576 expression until the time that the majority of cells in the well were surmised to be dead, GFP
577 expression could no longer be detected, or early termination was desired to permit Hoechst
578 staining.
579 In the case of PaKiT01 cells infected with rVSV-EBOV, where an apparently persistent
580 infection established, the assay was terminated after 200+ hours (8+ days) of continuous
581 observation. Upon termination of all trials, cells were fixed in formaldehyde (4% for 15 min),
582 incubated with Hoechst stain (0.0005% for 15 min) (ThermoFisher, Inc., Waltham, MA), then
583 imaged at 4X on the CellInsight CX5 High Content Screening (HCS) Platform. The machine was

allowed to find optimal focus for each Hoechst stain image. One color channel was permitted such that images produced showed live nuclei in white and dead cells in black.

Hoechst Staining.

Hoechst stain colors cellular DNA, and viral infection is thought to interfere with the clarity of the stain (Dembowski and DeLuca, 2015). As such, infection termination, cell fixation, and Hoechst staining enables generation of a rough time series of uninfectious live cells (i.e. susceptible + antiviral cells) to complement the images which produced time series of proportions infectious. Due to uncertainty over the exact epidemic state of Hoechst-stained cells (*i.e*. exposed but not yet infectious cells may still stain), we elected to fit our models only to the infectious time series derived from GFP-expressing images and used Hoechst stain images as a *post hoc* visual check on our fit only (Figure 5; Figure 5-figure supplement 1-2).

Image Processing.

Images recovered from the time series above were processed into binary ('infectious' vs. 'non-infectious' or, for Hoechst-stained images, 'live' vs. 'dead') form using the EBImage package (Pau et al. 2010) in R version 3.6 for MacIntosh, after methods further detailed in Supplementary File 7. Binary images were then further processed into time series of infectious or, for Hoechst-stained images, live cells using a series of cell counting scripts. Because of logistical constraints (i.e. many plates of simultaneously running infection trials and only one available imaging microscope), the time course of imaging across the duration of each trial was quite variable. As such, we fitted a series of statistical models to our processed image data to reconstruct reliable values of the infectious proportion of each well per hour for each distinct

607 trial in all cell line–virus-MOI combinations (Figure 1-figure supplement 2-3), as well as for
608 declining live cell counts from control well data derived from the Hoestch time series
609 (Supplementary File 1; Supplementary File 7; Figure 1-figure supplement 7). All original and
610 processed images, image processing and counting code, and resulting time series data are freely
611 available for download at the following FigShare repository: DOI:
612 10.6084/m9.figshare.8312807.
613
614 **Mean Field Model.**
615 *Theoretical Model Details*.
616 To derive the expression for R_0, the basic pathogen reproductive number *in vitro*, we
617 used Next Generation Matrix (NGM) techniques (Diekmann, Heesterbeek, and Metz 1990;
618 Heffernan, Smith, and Wahl 2005), employing Wolfram Mathematica (version 11.2) as an
619 analytical tool. R_0 describes the number of new infections generated by an existing infection in a
620 completely susceptible host population; a pathogen will invade a population when $R_0 >$
621 1 (Supplementary File 2). We then analyzed stability properties of the system, exploring
622 dynamics across a range of parameter spaces, using MatCont (version 2.2) (Dhooge et al. 2008)
623 for Matlab (version R2018a) (Supplementary File 3).
624
625 *Theoretical Model Fitting*.
626 The birth rate, b, and natural mortality rate, μ, balance to yield a population-level growth
627 rate, such that it is impossible to estimate both b and μ simultaneously from total population size
628 data alone. As such, we fixed b at .025 and estimated μ by fitting an infection-absent version of
629 our mean field model to the susceptible time series derived via Hoechst staining of control wells

630 for each of the three cell lines (Figure 1- figure supplement 7). This yielded a natural mortality
631 rate, μ, corresponding to a lifespan of approximately 121, 191, and 84 hours, respectively, for
632 Vero, RoNi/7.1, and PaKiT01 cell lines (Figure 1-figure supplement 7). We then fixed the virus
633 incubation rate, σ, as the inverse of the shortest observed duration of time from initial infection
634 to the observation of the first infectious cells via fluorescent microscope for all nine cell line –
635 virus combinations (ranging 6 to 9.5 hours). We fixed α, the infection-induced mortality rate, at
636 $\frac{1}{6}$, an accepted standard for general viral kinetics (Howat et al. 2006), and held *c,* the rate of
637 antiviral cell regression to susceptible status, at 0 for the timespan (<200 hours) of the
638 experimental cell line infection trials.

639 We estimated cell line–virus-MOI-specific values for β, ρ, and ε by fitting the
640 deterministic output of infectious proportions in our mean field model to the full suite of
641 statistical outputs of all trials for each infected cell culture time series (Figure 1-figure
642 supplement 2-3). Fitting was performed by minimizing the sum of squared differences between
643 the deterministic model output and cell line–virus-MOI-specific infectious proportion of the data
644 at each timestep. We optimized parameters for MOI = 0.001 and 0.0001 simultaneously to
645 leverage statistical power across the two datasets, estimating a different transmission rate, β, for
646 trials run at each infectious dose but, where applicable, estimating the same rates of ρ and ε
647 across the two time series. We used the differential equation solver lsoda() in the R package
648 deSolve (Soetaert, Petzoldt, and Setzer 2010) to obtain numerical solutions for the mean field
649 model and carried out minimization using the 'Nelder-Mead' algorithm of the optim() function
650 in base R. All model fits were conducted using consistent starting guesses for the parameters, β
651 (β= 3), and where applicable, ρ (ρ = 0.001) and ε (ε = 0.001). In the case of failed fits or

652 indefinite hessians, we generated a series of random guesses around the starting conditions and
653 continued estimation until successful fits were achieved.
654 All eighteen cell line–virus-MOI combinations of data were fit by an immune absent ($\varepsilon =$
655 $\rho = 0$) version of the theoretical model and, subsequently, an induced immunity ($\varepsilon = 0$; $\rho > 0$)
656 and constitutive immunity ($\varepsilon > 0$; $\rho > 0$) version of the model. Finally, we compared fits across
657 each cell line–virus-MOI combination via AIC. In calculating AIC, the number of fitted
658 parameters in each model (k) varied across the immune phenotypes, with one parameter (β)
659 estimated for absent immune assumptions, two (β and ρ) for induced immune assumptions, and
660 three (β, ρ, and ε) for constitutive immune assumptions. The sample size (n) corresponded to the
661 number of discrete time steps across all empirical infectious trials to which the model was fitted
662 for each cell-line virus combination. All fitting and model comparison script is freely available
663 for download at the following FigShare repository: DOI: 685 10.6084/m9.figshare.8312807.
664
665 *Spatial Model Simulations*.
666 Finally, we verified all mean field fits in a spatial context, in order to more thoroughly
667 elucidate the role of antiviral cells in each time series. We constructed our spatial model in C++
668 implemented in R using the packages Rcpp and RcppArmadillo (Eddelbuettel and Francois
669 2011; Eddelbuettel and Sanderson 2017). Following Nagai and Honda (2001) and Howat et al.
670 (2006), we modeled this system on a two-dimensional hexagonal lattice, using a ten-minute
671 epidemic timestep for cell state transitions. At the initialization of each simulation, we randomly
672 assigned a duration of natural lifespan, incubation period, infectivity period, and time from
673 antiviral to susceptible status to all cells in a theoretical monolayer. Parameter durations were
674 drawn from a normal distribution centered at the inverse of the respective fixed rates of μ, σ, α,

675 and c, as reported with our mean field model. Transitions involving the induced (ρ) and
676 constitutive (ε) rates of antiviral acquisition were governed probabilistically and adjusted
677 dynamically at each timestep based on the global environment. As such, we fixed these
678 parameters at the same values estimated in the mean field model, and multiplied both ρ and ε by
679 the global proportion of, respectively, exposed and susceptible cells at a given timestep.
680 In contrast to antiviral acquisition rates, transitions involving the birth rate (b) and the
681 transmission rate (β) occurred probabilistically based on each cell's local environment. The birth
682 rate, b, was multiplied by the proportion of susceptible cells within a six-neighbor circumference
683 of a focal dead cell, while β was multiplied by the proportion of infectious cells within a thirty-
684 six neighbor vicinity of a focal susceptible cell, thus allowing viral transmission to extend
685 beyond the immediate nearest-neighbor boundaries of an infectious cell. To compensate for
686 higher thresholds to cellular persistence and virus invasion which occur under local spatial
687 conditions (Webb, Keeling, and Boots 2007), we increased the birth rate, b, and the cell-to-cell
688 transmission rate, β, respectively, to six and ten times the values used in the mean field model
689 (Supplementary File 4). We derived these increases based on the assumption that births took
690 place exclusively based on pairwise nearest-neighbor interactions (the six immediately adjacent
691 cells to a focal dead cell), while viral transmission was locally concentrated but included a small
692 (7.5%) global contribution, representing the thirty-six cell surrounding vicinity of a focal
693 susceptible. We justify these increases and derive their origins further in Supplementary File 5.
694 We simulated ten stochastic spatial time series for all cell-virus combinations under all
695 three immune assumptions at a population size of 10,000 cells and compared model output with
696 data in Figure 5-figure supplement 3. Spatial model code is available for public access at the
697 following FigShare repository: DOI: 10.6084/m9.figshare.8312807.
698

Acknowledgments

CEB was supported by a National Science Foundation Graduate Research Fellowship at Princeton University and a Miller Institute for Basic Research Fellowship at UC Berkeley. Tissue culture experiments were funded by an NIH grant R01 AI134824 to KC. Work in LFW's lab was funded by the Singapore National Research Foundation grants (NRF2012NRF-CRP001-056 and NRF2016NRF-NSFC002-013). CD was supported by the German Research Council (DFG) grant DFG SPP1596 (DR 772/10–2), the Federal Ministry of Education and Research (BMBF) grant RAPID (#01KI1723A) and the EU Horizon 2020 grant EVAg (#653316). The authors thank the Chandran lab at Albert Einstein College of Medicine – in particular, Cecilia Harold, Megan Slough, Rohit Jangra, and Tanwee Alkutkar – for technical support during tissue culture experiments. The authors further thank Jessica Metcalf and the Graham lab at Princeton for conceptual guidance throughout the project's development.

722 **References**

723 Ahn, Matae, Danielle E. Anderson, Qian Zhang, Chee Wah Tan, Beng Lee Lim, Katarina Luko,
724 Ming Wen, et al. 2019. "Dampened NLRP3-Mediated Inflammation in Bats and
725 Implications for a Special Viral Reservoir Host." *Nature Microbiology* 4: 789–99.
726 https://doi.org/10.1038/s41564-019-0371-3.

727 Arnold, Catherine E, Jonathan C Guito, Louis A Altamura, Sean P Lovett, Elyse R Nagle,
728 Gustavo F Palacios, and Mariano Sanchez-lockhart. 2018. "Transcriptomics Reveal
729 Antiviral Gene Induction in the Egyptian Rousette Bat Is Antagonized in Vitro by Marburg
730 Virus Infection." *Viruses* 10 (607). https://doi.org/10.3390/v10110607.

731 Baccam, Prasith, Catherine Beauchemin, Catherine A Macken, Frederick G Hayden, and Alan S
732 Perelson. 2006. "Kinetics of Influenza A Virus Infection in Humans." *Journal of Virology*
733 80 (15): 7590–99. https://doi.org/10.1128/JVI.01623-05.

734 Biesold, Susanne E., Daniel Ritz, Florian Gloza-Rausch, Robert Wollny, Jan Felix Drexler,
735 Victor M. Corman, Elisabeth K V Kalko, Samuel Oppong, Christian Drosten, and Marcel
736 A. Müller. 2011. "Type I Interferon Reaction to Viral Infection in Interferon-Competent,
737 Immortalized Cell Lines from the African Fruit Bat Eidolon Helvum." *PLoS ONE* 6 (11).
738 https://doi.org/10.1371/journal.pone.0028131.

739 Bonhoeffer, S., R. M. May, G. M. Shaw, and M. A. Nowak. 1997. "Virus Dynamics and Drug
740 Therapy." *Proceedings of the National Academy of Sciences* 94 (13): 6971–76.
741 https://doi.org/10.1073/pnas.94.13.6971.

742 Brook, Cara E., and Andrew P. Dobson. 2015. "Bats as 'special' Reservoirs for Emerging
743 Zoonotic Pathogens." *Trends in Microbiology* 23 (3): 172–80.
744 https://doi.org/10.1016/j.tim.2014.12.004.

745 Brook, Cara E., Hafaliana Christian Ranaivoson, Christopher C. Broder, Andrew A.
746 Cunningham, Jean-Michel Héraud, Alison J. Peel, Louise Gibson, James L.N. Wood, C.
747 Jessica Metcalf, and Andrew P. Dobson. 2019. "Disentangling Serology to Elucidate
748 Henipa- and Filovirus Transmission in Madagascar Fruit Bats." *Journal of Animal Ecology*
749 00: 1– 16. https://doi.org/10.1111/1365-2656.12985.
750 Calisher, Charles H, James E Childs, Hume E Field, Kathryn V Holmes, and Tony Schountz.
751 2006. "Bats: Important Reservoir Hosts of Emerging Viruses." *Clinical Microbiology*
752 *Reviews* 19 (3): 531–45. https://doi.org/10.1128/CMR.00017-06.
753 Coffin, John M. 1995. "HIV Population Dynamics in Vivo: Implications for Genetic Variation,
754 Pathogenesis, and Therapy." *Science (New York, N.Y.)* 267 (5197): 483–89.
755 Crameri, Gary, Shawn Todd, Samantha Grimley, Jennifer A. McEachern, Glenn A. Marsh, Craig
756 Smith, Mary Tachedjian, et al. 2009. "Establishment, Immortalisation and Characterisation
757 of Pteropid Bat Cell Lines." *PLoS ONE* 4 (12): e8266.
758 https://doi.org/10.1371/journal.pone.0008266.
759 Desmyter, J, J L Melnick, and W E Rawls. 1968. "Defectiveness of Interferon Production and of
760 Rubella Virus Interference in a Line of African Green Monkey Kidney Cells (Vero)."
761 *Journal of Virology* 2 (10): 955–61. https://doi.org/J. Virol. 1968 2:1955.
762 Dhooge, A., W. Govaerts, Yu A. Kuznetsov, H. G E Meijer, and B. Sautois. 2008. "New
763 Features of the Software MatCont for Bifurcation Analysis of Dynamical Systems."
764 *Mathematical and Computer Modelling of Dynamical Systems* 14 (2): 147–75.
765 https://doi.org/10.1080/13873950701742754.
766 Diekmann, O., J.A.P. Heesterbeek, and J.A.J Metz. 1990. "On the Definition and Computation of
767 the Basic Reproduction Ratio R0 in Models for Infectious Diseases in Heterogenous

Populations." *Journal of Mathematical Biology* 28: 365–82.

Eddelbuettel, Dirk, and Romain Francois. 2011. "Rcpp: Seamless R and C++ Integration." *Journal of Statistical Software* 40: 1–18. https://doi.org/10.1007/978-1-4614-6868-4.

Eddelbuettel, Dirk, and Conrad Sanderson. 2017. "RcppArmadillo: Accelerating R with High-Performance C++ Linear Algebra." *Computational Statistics and Data Analysis* 71 (2014): 1–16.

Emeny, J. M., and M. J. Morgan. 1979. "Regulation of the Interferon System: Evidence That Vero Cells Have a Genetic Defect in Interferon Production." *Journal of General Virology* 43 (1): 247–52. https://doi.org/10.1099/0022-1317-43-1-247.

Emery, V.C., A.V. Cope, E.F. Bowen, D. Gor, and P.D. Griffiths. 1999. "The Dynamics of Human Cytomegalovirus Replication in Vivo." *The Journal of Experimental Medicine* 190 (2): 177–82. https://doi.org/10.1084/jem.190.2.177.

Haydon, Daniel T, Sarah Cleaveland, Louise H Taylor, and M Karen Laurenson. 2002. "Identifying Reservoirs of Infection: A Conceptual and Practical Challenge." *Emerging Infectious Diseases* 8 (12): 1468–73. https://doi.org/10.3201/eid0812.010317.

Heffernan, J.M., R.J. Smith, and L.M. Wahl. 2005. "Perspectives on the Basic Reproductive Ratio." *Journal of The Royal Society Interface* 2 (4): 281–93. https://doi.org/10.1098/rsif.2005.0042.

Ho, David D., Avidan U. Neumann, Alan S. Perelson, Wen Chen, John M. Leonard, and Martin Markowitz. 1995. "Rapid Turnover of Plasma Virions and CD4 Lymphocytes in HIV-1 Infection." *Nature* 373: 123–26. https://doi.org/10.1038/373123a0.

Hooper, Peter, Sherif Zaki, Peter Daniels, and Deborah Middleton. 2001. "Comparative Pathology of the Diseases Caused by Hendra and Nipah Viruses." *Microbes and Infection* 3

791 (4): 315–22. https://doi.org/10.1016/S1286-4579(01)01385-5.

792 Howat, Tom J, Cristina Barreca, Peter O'Hare, Julia R Gog, and Bryan T Grenfell. 2006.
793 "Modelling Dynamics of the Type I Interferon Response to in Vitro Viral Infection."
794 *Journal of the Royal Society, Interface* 3 (10): 699–709.
795 https://doi.org/10.1098/rsif.2006.0136.

796 Igarashi, Manabu, Heinz Feldmann, Yoshihiro Takadate, Tatsunari Kondoh, Manabu Igarashi,
797 Junki Maruyama, Rashid Manzoor, and Hirohito Ogawa. 2020. "Niemann-Pick C1
798 Heterogeneity of Bat Cells Controls Filovirus Tropism." *Cell Reports* 30 (2): 308-319.e5.
799 https://doi.org/10.1016/j.celrep.2019.12.042.

800 Kacprzyk, Joanna, Graham M. Hughes, Eva M. Palsson-McDermott, Susan R. Quinn, Sébastien
801 J. Puechmaille, Luke A. J. O'Neill, and Emma C. Teeling. 2017. "A Potent Anti-
802 Inflammatory Response in Bat Macrophages May Be Linked to Extended Longevity and
803 Viral Tolerance." *Acta Chiropterologica* 19 (2): 219–28.
804 https://doi.org/10.3161/15081109ACC2017.19.2.001.

805 Keeling, Matt J., and Pejman Rohani. 2008. *Modeling Infectious Diseases in Humans and*
806 *Animals*. Princeton, NJ: Princeton University Press.

807 Kühl, Annika, Markus Hoffmann, Marcel A. Müller, Vincent J. Munster, Kerstin Gnirß, Miriam
808 Kiene, Theodros Solomon Tsegaye, et al. 2011. "Comparative Analysis of Ebola Virus
809 Glycoprotein Interactions with Human and Bat Cells." *Journal of Infectious Diseases* 204:
810 S840–S849. https://doi.org/10.1093/infdis/jir306.

811 Kuzmin, I.V., Toni M. Schwarz, Philipp A. Ilinykh, Ingo Jordan, Thamas G. Ksiazek, Ravi
812 Sachidanandam, Christopher F. Basler, and Alexander Bukreyev. 2017. "Innate Immune
813 Response of Bat and Human Cells to Filoviruses: Commonalities and Distinctions." *Journal*

814 *of Virology* 91 (8): e02471-16. https://doi.org/10.1128/JVI.02471-16.

815 Livak, K J, and T D Schmittgen. 2001. "Analysis of Relative Gene Expression Data Using Real-
816 Time Quantitative PCR and the 2^(-ΔΔCT) Method." *Methods* 25 (4): 402–8.
817 https://doi.org/10.1006/meth.2001.1262.

818 Mahanty, Siddhartha, and Mike Bray. 2004. "Pathogenesis of Filoviral Haemorrhagic Fevers."
819 *Lancet Infectious Diseases* 4 (8): 487–98. https://doi.org/10.1016/S1473-3099(04)01103-X.

820 Miller, Emily Happy, Gregor Obernosterer, Matthijs Raaben, Andrew S Herbert, Maika S
821 Deffieu, Anuja Krishnan, Esther Ndungo, et al. 2012. "Ebola Virus Entry Requires the
822 Host-Programmed Recognition of an Intracellular Receptor." *The EMBO Journal* 31 (8):
823 1947–60. https://doi.org/10.1038/emboj.2012.53.

824 Morris, Sinead E., Andrew J. Yates, Rik L. de Stwart, Rory D. de Vries, Michael J. Mina, Ashley
825 N. Nelson, Wen-Hsuan W. Lin, Roger D. Kouyos, Diane E. Griffin, and Bryan T. Grenfell.
826 2018. "Modeling the Measles Paradox Reveals the Importance of Cellular Immunity in
827 Regulating Viral Clearance." *PLoS Pathogens* 14 (12): e1007493.

828 Neumann, AU, NP Lam, H Dahari, DR Gretch, TE Wiley, TJ Layden, and AS Perelson. 1998.
829 "Hepatitis C Viral Dynamics in Vivo and the Antiviral Efficacy of Interferon-Alpha
830 Therapy." *Science* 282: 103–7.

831 Ng, Melinda, and Kartik Chandran. 2018. "Unpublished Results."

832 Ng, Melinda, Esther Ndungo, Maryska Kaczmarek, Andrew S. Herbert, Tabea Binger, Rebekah
833 James, Rohit K. Jangra, et al. 2015. "NPC1 Contributes to Species-Specific Patterns of
834 Ebola Virus Infection in Bats." *ELife* 4: e11785. https://doi.org/10.7554/eLife.11785.

835 Nicholls, J M, L L Poon, K C Lee, W F Ng, S T Lai, C Y Leung, C M Chu, et al. 2003. "Lung
836 Pathogy of Fatal Severe Acute Respiratory Syndrom." *Lancet* 361: 1773–78.

837 https://doi.org/10.1016/S0140-6736(03)13413-7.

838 Nowak, M. A., and R. M. May. 2000. *Virus Dynamics: Mathematical Principles of Immunology*
839 *and Virology*. Oxford, UK: Oxford University Press.

840 Nowak, Martin A., Robert M. May, Rodney E. Phillips, Sarah Rowland-Jones, David G. Lalloo,
841 Steven McAdam, Paul Klenerman, et al. 1995. "Antigenic Oscillations and Shifting
842 Immunodominance in HIV-1 Infections." *Nature* 375: 606–11.

843 Nowak, Martin A, Sebastian Bonhoeffer, Andrew M Hill, Richard Boehme, Howard C Thomas,
844 and Hugh McDade. 1996. "Viral Dynamics in Hepatitis B Virus Infection." *Proceedings of*
845 *the National Academy of Sciences* 93: 4398–4402.
846 http://www.pnas.org/content/pnas/93/9/4398.full.pdf.

847 Pau, Gregoire, Florian Fuchs, Oleg Sklyar, Michael Boutros, and Wolfgang Huber. 2010.
848 "EBImage-an R Package for Image Processing with Applications to Cellular Phenotypes."
849 *Bioinformatics* 26 (7): 979–81. https://doi.org/10.1093/bioinformatics/btq046.

850 Pavlovich, Stephanie S., Sean P. Lovett, Galina Koroleva, Jonathan C. Guito, Catherine E.
851 Arnold, Elyse R. Nagle, Kirsten Kulcsar, et al. 2018. "The Egyptian Rousette Genome
852 Reveals Unexpected Features of Bat Antiviral Immunity." *Cell* 173 (5): 1098–1110.
853 https://doi.org/10.1016/j.cell.2018.03.070.

854 Pawelek, Kasia A., Giao T. Huynh, Michelle Quinlivan, Ann Cullinane, Libin Rong, and Alan S.
855 Perelson. 2012. "Modeling Within-Host Dynamics of Influenza Virus Infection Including
856 Immune Responses." *PLoS Computational Biology* 8 (6): e1002588.
857 https://doi.org/10.1371/journal.pcbi.1002588.

858 Peel, Alison J., Kate S. Baker, David T. S. Hayman, Christopher C. Broder, Andrew A.
859 Cunningham, Anthony R. Fooks, Romain Garnier, James L. N. Wood, and Olivier Restif.

860 2018. “Support for Viral Persistence in Bats from Age-Specific Serology and Models of
861 Maternal Immunity.” *Scientific Reports* 8 (1): 3859. https://doi.org/10.1038/s41598-018-
862 22236-6.
863 Peel, Alison J, Kate S Baker, Gary Crameri, Jennifer A Barr, David TS Hayman, Edward
864 Wright, Christopher C Broder, et al. 2012. “Henipavirus Neutralising Antibodies in an
865 Isolated Island Population of African Fruit Bats.” *PloS One* 7 (1): e30346.
866 https://doi.org/10.1371/journal.pone.0030346.
867 Perelson, A S, A U Neumann, M Markowitz, J M Leonard, and D D Ho. 1996. “HIV-1
868 Dynamics in Vivo: Virion Clearance Rate, Infected Cell Life-Span, and Viral Generation
869 Time.” *Science (New York, N.Y.)* 271 (5255): 1582–86.
870 https://doi.org/10.1126/science.271.5255.1582.
871 Perelson, Alan S. 2002. “Modelling Viral and Immune System Dynamics.” *Nature Reviews*
872 *Immunology* 2 (1): 28–36. https://doi.org/10.1038/nri700.
873 Plowright, Raina K., Alison J. Peel, Daniel G. Streicker, Amy Gilbert, Hamish McCallum, James
874 Wood, Michelle L. Baker, and Olivier Restif. 2016. “Transmission or Within-Host
875 Dynamics Driving Pulses of Zoonotic Viruses in Reservoir-Host Populations.” *PLoS*
876 *Neglected Tropical Diseases* 10 (8): e0004796.
877 https://doi.org/10.1371/journal.pntd.0004796.
878 Radke, K L, C Colby, J R Kates, H M Krider, and D M Prescott. 1974. “Establishment and
879 Maintenance of the Interferon-Induced Antiviral State: Studies in Enucleated Cells.”
880 *Journal of Virology* 13 (3): 623–30.
881 http://www.ncbi.nlm.nih.gov/pubmed/4362865%0Ahttp://www.pubmedcentral.nih.gov/arti
882 clerender.fcgi?artid=PMC355347.

883 Rasmussen, L., and L. B. Farley. 1975. “Inhibition of *Herpesvirus Hominis* Replication by
884 Human Interferon.” *Infection and Immunity* 12 (1): 104–8.
885 Rhim, J. S., K. Schell, B. Creasy, and W. Case. 1969. “Biological Characteristics and Viral
886 Susceptibility of an African Green Monkey Kidney Cell Line (Vero).” *Proceedings of the*
887 *Society for Experimental Biology and Medicine* 132 (2): 670-678.
888 Saenz, Roberto A, Michelle Quinlivan, Debra Elton, Shona MacRae, Anthony S Blunden,
889 Jennifer A Mumford, Janet M Daly, et al. 2010. “Dynamics of Influenza Virus Infection and
890 Pathology.” *Journal of Virology* 84 (8): 3974–83. https://doi.org/10.1128/JVI.02078-09.
891 Samuel, C. E., and G. S. Knutson. 1982. “Mechanism of Interferon Action.” *Journal of*
892 *Biological Chemistry* 257 (19): 11791–95.
893 Schountz, Tony, Michelle L Baker, John Butler, and Vincent Munster. 2017. “Immunological
894 Control of Viral Infections in Bats and the Emergence of Viruses Highly Pathogenic to
895 Humans.” *Frontiers in Immunology* 8 (September): Article 1098.
896 https://doi.org/10.3389/fimmu.2017.01098.
897 Soetaert, Karline, Thomas Petzoldt, and R Woodrow Setzer. 2010. “Package DeSolve: Solving
898 Initial Value Differential Equations in R.” *Journal of Statistical Software* 33 (9): 1–25.
899 https://doi.org/10.18637/jss.v033.i09.
900 Stetson, Daniel B., and Ruslan Medzhitov. 2006. “Type I Interferons in Host Defense.” *Immunity*
901 25 (3): 373–81. https://doi.org/10.1016/j.immuni.2006.08.007.
902 Team, R Core. 2019. “R: A Language and Environment for Statistical Computing.” *R*
903 *Foundation for Statistical Computing*. Vienna, Austria.
904 Wang, Lin-Fa, and Danielle E Anderson. 2019. “Viruses in Bats and Potential Spillover to
905 Animals and Humans.” *Current Opinion in Virology* 34: 79–89.

https://doi.org/10.1016/j.coviro.2018.12.007.

Webb, Steven D., Matt J. Keeling, and Mike Boots. 2007. "Host-Parasite Interactions between the Local and the Mean-Field: How and When Does Spatial Population Structure Matter?" *Journal of Theoretical Biology* 249 (1): 140–52. https://doi.org/10.1016/j.jtbi.2007.06.013.

Wong, Anthony C, Rohini G Sandesara, Nirupama Mulherkar, Sean P Whelan, and Kartik Chandran. 2010. "A Forward Genetic Strategy Reveals Destabilizing Mutations in the Ebolavirus Glycoprotein That Alter Its Protease Dependence during Cell Entry." *Journal of Virology* 84 (1): 163–75. https://doi.org/10.1128/JVI.01832-09.

Xie, Jiazheng, Yang Li, Xurui Shen, Jiazheng Xie, Yang Li, Xurui Shen, Geraldine Goh, et al. 2018. "Dampened STING-Dependent Interferon Activation in Bats." *Cell Host and Microbe* 23: 297–301.

Zhang, Guojie, Christopher Cowled, Zhengli Shi, Zhiyong Huang, Kimberly a Bishop-Lilly, Xiaodong Fang, James W Wynne, et al. 2013. "Comparative Analysis of Bat Genomes Provides Insight into the Evolution of Flight and Immunity." *Science* 339 (6118): 456–60. https://doi.org/10.1126/science.1230835.

Zhou, Peng, Mary Tachedjian, James W Wynne, Victoria Boyd, Jie Cui, Ina Smith, Christopher Cowled, et al. 2016. "Contraction of the Type I IFN Locus and Unusual Constitutive Expression of IFN-α in Bats." *Proceedings of the National Academy of Sciences* 113 (10): 2696–2701. https://doi.org/10.1073/pnas.1518240113.

929 **Tables**

930 **Table 1. Optimized parameters from best fit deterministic model and spatial approximation at MOI=.001**

Cell Line	Virus	Immune Assumption	δ AIC Reduction†	Antiviral Rate	ε [lci – uci] *	ρ [lci – uci] *	β [lci – uci] *	mean field R_0	spatial β
Vero	rVSV-G	Absent	2	0	0 [0-0]	0 [0-0]	2.44 [1.52-3.36]	8.73	24.418
	rVSV-EBOV	Absent	2	0	0 [0-0]	0 [0-0]	1.5 [1.06-1.94]	5.42	14.996
	rVSV-MARV	Absent	2	0	0 [0-0]	0 [0-0]	0.975 [0.558-1.39]	3.45	9.752
RoNi/7.1	rVSV-G	Induced	2	7.03×10^{-5}	0 [0-0]	0.089 [0-0.432]	2.47 [1.49-3.45]	10.91	24.705
	rVSV-EBOV	Induced	2.01	2.87×10^{-5}	0 [0-0]	0.0363 [0-0.343]	0.685 [0.451-0.919]	3.04	6.849
	rVSV-MARV	Induced	2	1.40×10^{-5}	0 [0-0]	0.0177 [0-0.257]	1.23 [0.917-1.55]	5.48	12.324
PaKiT01	rVSV-G	Constitutive	29.9	.00209	0.00602 [0-0.019]	8.26×10^{-8} [0-4.75 $\times 10^{-7}$]	3.45 [1.07-5.84]	6.20	34.516
	rVSV-EBOV	Constitutive	27.9	.00499	0.0478 [0-0.0958]	4.46×10^{-8} [0-4.37 $\times 10^{-7}$]	34.5 [28.7-40.2]	18.82	344.821
	rVSV-MARV	Induced	2	.00687	0 [0-0]	13.1 [0-37.9]	3.25 [0-41.3]	8.83	32.452

931 †Improvement in AIC from next best model for same cell line-virus-MOI combination. All δ-AIC are reported in Supplementary File 4.
932 * lci = lower and uci = upper 95% confidence interval. No confidence interval is shown for spatial β which was fixed at 10 times the estimated
933 mean for the mean field model fits when paired with equivalent values of ε and ρ.
934 All other parameters were fixed at: b=.025 (mean field), 0.15 (spatial); α = 1/6; c=0; μ= 1/121 (Vero), 1/191 (RoNi/7.1), and 1/84 (PaKiT01)
935
936
937
938
939
940
941
942
943
944

945 **Main Figure Captions**

946 **Figure 1.** Fitted time series of infectious cell proportions from mean field model for rVSV-G,
947 rVSV-EBOV, and rVSV-MARV infections (columns) on Vero, RoNi/7.1, and PaKiT01 cell
948 lines (rows) at MOI=0.001. Results are shown for the best fit immune absent model on Vero
949 cells, induced immunity model on RoNi/7.1 cells, and constitutive (for rVSV-VSVG and rVSV-
950 EBOV) and induced (for rVSV-MARV) immunity models on PaKiT01 cells. Raw data across all
951 trials are shown as open circles (statistical smoothers from each trial used for fitting are available
952 in Figure 1-figure supplement 2-3). Model output is shown as a solid crimson line (95%
953 confidence intervals by standard error = red shading). Panel background corresponds to
954 empirical outcome of the average stochastic cell culture trial (persistent infection = white; virus-
955 induced epidemic extinction = gray; immune-mediated epidemic extinction = black). Parameter
956 values are listed in Table 1 and Supplementary File 4. Results for absent/induced/constitutive
957 fitted models across all cell lines are shown in Figure 1-figure supplement 4 (MOI=0.001) and
958 Figure 1-figure supplement 5 (MOI=0.0001).

959

960 **Figure 2.** Two parameter bifurcations of the mean field model, showing variation in the
961 transmission rate, β, against variation in the pathogen-induced mortality rate, α, under diverse
962 immune assumptions. Panel (A) depicts dynamics under variably constitutive immunity, ranging
963 from absent (left: $\varepsilon = 0$) to high (right: $\varepsilon = .0025$). In all panel (A) plots, the rate of induced
964 immune antiviral acquisition (ρ) was fixed at 0.01. Panel (B) depicts dynamics under variably
965 induced immunity, ranging from absent (left: ρ=0) to high (right: ρ=1). In all panel (B) plots, the
966 rate of constitutive antiviral acquisition (ε) was fixed at 0.0001. Branch point curves are
967 represented as solid lines and Hopf curves as dashed lines. White space indicates endemic

968 equilibrium (persistence), gray space indicates limit cycles, and black space indicates no
969 infection (extinction). Other parameter values for equilibrium analysis were fixed at: b = .025, μ
970 = .001, σ = 1/6, c = 0. Special points from bifurcations analyses are listed in Supplementary File
971 3.
972
973 **Figure 3.** Two parameter bifurcations of the mean field model, showing variation in the
974 transmission rate, β, against variation in: (A) the induced immunity rate of antiviral acquisition
975 (ρ) and (B) the constitutive immunity rate of antiviral acquisition (ε). Panels show variation in
976 the extent of immunity, from absent (left) to high (right). Branch point curves are represented as
977 solid lines and Hopf curves as dashed lines. White space indicates endemic equilibrium
978 (persistence), gray space indicates limit cycling, and black space indicates no infection
979 (extinction). Other parameter values for equilibrium analysis were fixed at: b = .025, μ = .001, σ
980 = 1/6, α = 1/6, c = 0. Special points from bifurcations analyses are listed in Supplementary File
981 3.
982
983 **Figure 4.** Best fit parameter estimates for β and ρ or ε from mean-field model fits to MOI=0.001
984 time series data, atop (A,B) $\beta - \rho$ and (C) $\beta - \varepsilon$ bifurcation. Fits and bifurcations are grouped by
985 immune phenotype: (A) absent; (B) induced; (C) constitutive immunity, with cell lines differentiated
986 by shape (Vero=circles; RoNi/7.1 = triangles; PaKiT01=squares) and viral infections by color
987 (rVSV-G = green, rVSV-EBOV = magenta, rVSV-MARV = blue). Note that y-axis values are ten-
988 fold higher in panel (C). Branch point curves (solid lines) and Hopf curves (dashed lines) are
989 reproduced from Figure 3. White space indicates endemic equilibrium (pathogen persistence), gray
990 space indicates limit cycling (virus-induced epidemic extinction), and black space indicates no

991 infection (immune-mediated pathogen extinction). In panel (A) and (B), ε is fixed at 0; in panel (C),
992 ρ is fixed at $5x10^{-8}$ for bifurcation curves and estimated at $4x10^{-8}$ and $8x10^{-8}$ for rVSV-EBOV and
993 rVSV-G parameter points, respectively. Other parameter values were fixed at: b = .025, μ = 0.001, σ
994 = 1/6, α = 1/6, and c = 0 across all panels. Raw fitted values and corresponding 95% confidence
995 intervals for β, ρ, and ε, background parameter values, and AIC recovered from model fit, are
996 reported in Supplementary File 4. Parameter fits at MOI=0.0001 are visualized in Figure 4-figure
997 supplement 1.
998
999 **Figure 5.** Fitted time series of susceptible (green shading) and antiviral (blue shading) cell
1000 proportions from the mean field model for rVSV-G, rVSV-EBOV, and rVSV-MARV infections
1001 (columns) on Vero, RoNi/7.1, and PaKiT01 cell lines (rows) at MOI=0.001. Results are shown
1002 for the best fit immune absent model on Vero cells, induced immunity model on RoNi/7.1 cells
1003 and constitutive (rVSV-G and rVSV-EBOV) and induced (rVSV-MARV) immune models on
1004 PaKiT01 cells. Combined live, uninfectious cell populations (S + A + E) are shown in tan
1005 shading, with raw live, uninfectious cell data from Hoechst stains visualized as open circles. The
1006 right-hand y-axis corresponds to R-effective (pink solid line) across each time series; R-effective
1007 =1 is a pink dashed, horizontal line. Panel background corresponds to empirical outcome of the
1008 average stochastic cell culture trial (persistent infection = white; virus-induced epidemic
1009 extinction = gray; immune-mediated epidemic extinction = black). Parameter values are listed in
1010 Supplementary File 4 and results for absent/induced/constitutive fitted models across all cell
1011 lines in Figure 5-figure supplement 1 (MOI=0.001) and Figure 5-figure supplement 2
1012 (MOI=0.0001).
1013

1014 **Figure Supplement Captions**

1015 **Figure 1 – figure supplement 1.** Cell culture models of viral propagation. (A), (B), and (C)
1016 show raw, original images of rVSV-EBOV propagation across Vero cell lines at, respectively,
1017 17, 21, and 28 hours post-infection (timesteps 2, 3, and 5 from trial Ver6_B1). (D), (E), and (F)
1018 show corresponding, binary images processed in the R package, EBImage. Cells expressing viral
1019 eGFP are depicted in white and uninfected/dead cells in black.

1020

1021 **Figure 1 – figure supplement 2.** Time series data to which mean field mechanistic models were
1022 fit, across rVSV-G (left), rVSV-EBOV (middle), and rVSV-MARV (right) infections on Vero,
1023 RoNi/7.1, and PaKiT01 cell lines, at MOI=0.001. Open circles show raw data across all trials,
1024 while red, dashed line gives the statistical mean of each trials, established from GAM model
1025 incorporating random effects per trial. Results for MOI=0.0001 are shown in Figure 1 – figure
1026 supplement 3.

1027

1028 **Figure 1 – figure supplement 3.** Time series data to which mean field mechanistic models were
1029 fit, across rVSV-G (left), rVSV-EBOV (middle), and rVSV-MARV (right) infections on Vero,
1030 RoNi/7.1, and PaKiT01 cell lines, at MOI=0.0001. Open circles show raw data across all trials,
1031 while red, dashed line gives the statistical mean of each trials, established from GAM model
1032 incorporating random effects per trial. Results for MOI=0.001 are shown in Figure 1 – figure
1033 supplement 2.

1034

1035 **Figure 1 – figure supplement 4.** Figure replicates Figure 1 (main text) but includes all output
1036 across mean field model fits assuming (A) absent immunity, (B) induced immunity, and (C)

1037 constitutive immunity. Figure shows fitted time series of infectious cell proportions for rVSV-G,
1038 rVSV-EBOV, and rVSV-MARV infections (columns) on Vero, RoNi/7.1, and PaKiT01 cell
1039 lines (rows) at MOI=0.001. Raw data across all trials are shown as open circles and model output
1040 as the solid crimson line (95% confidence intervals by standard error = red shading). Panel
1041 background corresponds to empirical outcome of the average stochastic cell culture trial
1042 (persistent infection = white; virus-induced epidemic extinction = gray; immune-mediated
1043 epidemic extinction = black).
1044
1045 **Figure 1 – figure supplement 5.** Figure replicates Figure 1 – figure supplement 4 exactly but
1046 shows model fits and data for all cell-virus combinations at MOI=0.0001.
1047
1048 **Figure 1 – figure supplement 6.** (A) IFN-α and (B) IFN-β gene expression profiles from qPCR
1049 for rVSV infections on RoNi/7.1 and PaKiT01 cell lines. Panels show δ-Ct (raw Ct of IFN gene
1050 assay subtracted from raw Ct of β-Actin housekeeping gene assay) across a time series for mock
1051 (left), MOI=0.0001 (middle) and MOI=0.001 (right) infections across a time series. Viruses are
1052 represented by color (rVSV-G=green, rVSV-EBOV=magenta, rVSV-MARV=blue). The red
1053 dashed line at δ-Ct=37 corresponds to no expression; higher expression is indicated at lower
1054 values for δ-Ct. qPCR was carried out using primers summarized in Supplementary File 6.
1055
1056 **Figure 1 – figure supplement 7.** Curve fits to control data for standard birth (b =.025) and
1057 natural mortality ($\mu = \frac{1}{121}, \frac{1}{191}, \frac{1}{84}$ hours for, respectively, Vero, RoNi/7.1, and PaKiT01 cell
1058 lines) rates across all three cell lines. Raw data from multiple trials are shown as open circles,

1059 statistical means as dashed black lines, with the output from the mean field model, using the
1060 fixed birth rate and estimated mortality rate, in solid green.
1061
1062 **Figure 4 – figure supplement 1.** Best fit parameter estimates for β and ρ or ε from mean-field
1063 model fits to MOI=0.0001 time series data, atop (A,B) β – ρ and (C) β – ε bifurcation. Fits and
1064 bifurcations are grouped by immune phenotype: (A) absent; (B) induced; (C) constitutive
1065 immunity, with cell lines differentiated by shape (Vero=circles; RoNi/7.1 = triangles;
1066 PaKiT01=squares) and viral infections by color (rVSV-G = green, rVSV-EBOV = magenta,
1067 rVSV-MARV = blue). Note that y-axis values are ten-fold higher in panel (C). Branch point
1068 curves (solid lines) and Hopf curves (dashed lines) are reproduced from Figure 3 (main text).
1069 White space indicates endemic equilibrium (pathogen persistence), gray space indicates limit
1070 cycling (virus-induced epidemic extinction), and black space indicates no infection (immune-
1071 mediated pathogen extinction). In panel (A) and (B), ε is fixed at 0; in panel (C), ε is fixed at
1072 $5x10^{-8}$ for bifurcation curves and estimated at $4x10^{-8}$ and $8x10^{-8}$ for rVSV-EBOV and rVSV-G
1073 parameter points, respectively. To construct bifurcation curves, other parameter values were
1074 fixed at: $b = 0.025$, $\mu = 0.001$, $\alpha = \frac{1}{6}$, and $c = 0$ across all panels. Raw fitted values and
1075 corresponding 95% confidence intervals for β, ρ, and ε, background parameter values, and AIC
1076 recovered from model fit, are reported in Supplementary File 4. Parameter fits at MOI=0.0001
1077 are visualized in Figure 4 of the main text.
1078
1079 **Figure 5 – figure supplement 1.** Figure replicates Figure 5 (main text) but includes all output
1080 across mean field model fits assuming (A) absent immunity, (B) induced immunity, and (C)
1081 constitutive immunity. Figure shows fitted time series of susceptible (green shading) and

1082 antiviral (blue shading) cell proportions from the mean field model for rVSV-G, rVSV-EBOV,
1083 and rVSV-MARV infections (columns) on Vero, RoNi/7.1, and PaKiT01 cell lines (rows) at
1084 MOI=0.001. Combined live, uninfectious cell populations (S + A + E, summed across the time
1085 series) is shown in tan shading, with raw live, uninfectious cell data from Hoechst stains of
1086 terminal time series visualized as open circles. The right-hand y-axis corresponds to R-effective
1087 (pink solid line) across each time series; R-effective = 1 is given as a pink dashed, horizontal
1088 line. Panel background corresponds to empirical outcome of the average stochastic cell culture
1089 trial (persistent infection = white; virus-induced epidemic extinction = gray; immune-mediated
1090 epidemic extinction = black).
1091
1092 **Figure 5 – figure supplement 2.** Figure replicates Figure 5 – figure supplement 1 exactly but
1093 shows model fits and data for all cell-virus combinations at MOI=0.0001.
1094
1095 **Figure 5 – figure supplement 3.** Spatial model state variable outputs, fit to MOI=0.001 data
1096 only, for all 27 unique cell line - virus - immune assumption combinations: (A) absent immunity,
1097 (B) induced immunity, and (C) constitutive immunity. Values for ρ and ε were fixed at
1098 equivalent values to those optimized in mean field trials and β fixed at ten times the value
1099 estimated under mean field conditions. Figure shows mean output from 10 runs of the spatial
1100 stochastic model, on a 10,000 cell lattice for MOI=0.001 infections of rVSV-G, rVSV-EBOV,
1101 and rVSV-MARV (columns) on Vero, RoNi/7.1, and PaKiT01 (rows) cell lines. Mean state
1102 variable outputs are plotted as colored lines with 95% confidence intervals by standard error
1103 shown in corresponding shading (infectious = red; susceptible = green; antiviral = blue). Raw
1104 infectious cell data across all time trials are plotted as open red circles, with the Hoechst-stained

1105 live cell population as open black circles. Modeled live, uninfectious cell populations (S+A+E)
1106 are shown in tan shading in the background. Panel background shading corresponds to the mean
1107 spatial model outcome for each cell line – virus combination (persistent infection = white; virus-
1108 induced epidemic extinction = gray; immune-mediated epidemic extinction = black). All
1109 parameter values are reported in Supplementary File 4.
1110
1111
1112
1113
1114
1115
1116
1117
1118
1119
1120
1121
1122
1123
1124
1125
1126
1127

1128 **Video Captions**

1129 **Video 1.** Two hundred hour time series of spatial stochastic model for rVSV-EBOV infection on
1130 10,000 cell grid for PaKiT01, assuming conditions of *absent immunity*: (A) spatial spread of
1131 infection, (B) time series of state variables. Parameter values are listed in Supplementary File 4.
1132

1133 Video 2. Two hundred hour time series of spatial stochastic model for rVSV-EBOV infection on
1134 10,000 cell grid for PaKiT01, assuming conditions of *induced immunity*: (A) spatial spread of
1135 infection, (B) time series of state variables. Parameter values are listed in Supplementary File 4.
1136

1137 Video 3. Two hundred hour time series of spatial stochastic model for rVSV-EBOV infection on
1138 10,000 cell grid for PaKiT01, assuming conditions of *constitutive immunity*: (A) spatial spread of
1139 infection, (B) time series of state variables. Parameter values are listed in Supplementary File 4.
1140
1141
1142
1143
1144
1145
1146
1147
1148
1149
1150

1151 **Supplementary File Captions**

1152 **Supplementary File 1.** (A) Raw proportion infectious from cell culture images. Dataset gives
1153 raw proportion of infectious cells and time elapsed for all trials of all cell line/virus/MOI
1154 combinations, derived from image processing of binary images. (B) Raw proportion uninfectious
1155 from cell culture images. Dataset gives raw proportion of uninfectious cells and time elapsed for
1156 all trials of all cell line/virus/MOI combinations, derived from image processing of binary
1157 Hoechst-stained images. (C) Statistical mean of infectious time series for all trials of each cell
1158 line/virus/MOI experiment, from GAM fitted model incorporating random effects by trial. Data
1159 were smoothed to yield the proportion infectious per hourly timestep for each trial, and mean
1160 field mechanistic models were fit to the smoothed mean of all compiled trials for each cell
1161 line/virus/MOI combination. (D) Statistical mean of uninfectious time series for all eighteen cell
1162 line/virus/MOI experiments, from generalized linear model fit to Hoechst stain data reported on
1163 tab B. Note that these means were not used in epidemic model fitting but natural mortality rates
1164 for each cell line were derived from fitting an infection-absent model to the trajectory of
1165 susceptible decline for control trials for each cell line, as shown in Figure 1 – figure supplement
1166 7. All original raw image files, processed binary images, and image processing code are
1167 available freely for download at the following FigShare repository: DOI:
1168 10.6084/m9.figshare.8312807.

1169

1170 **Supplementary Files 2-7** are all supplementary tables or text which do not require captions.

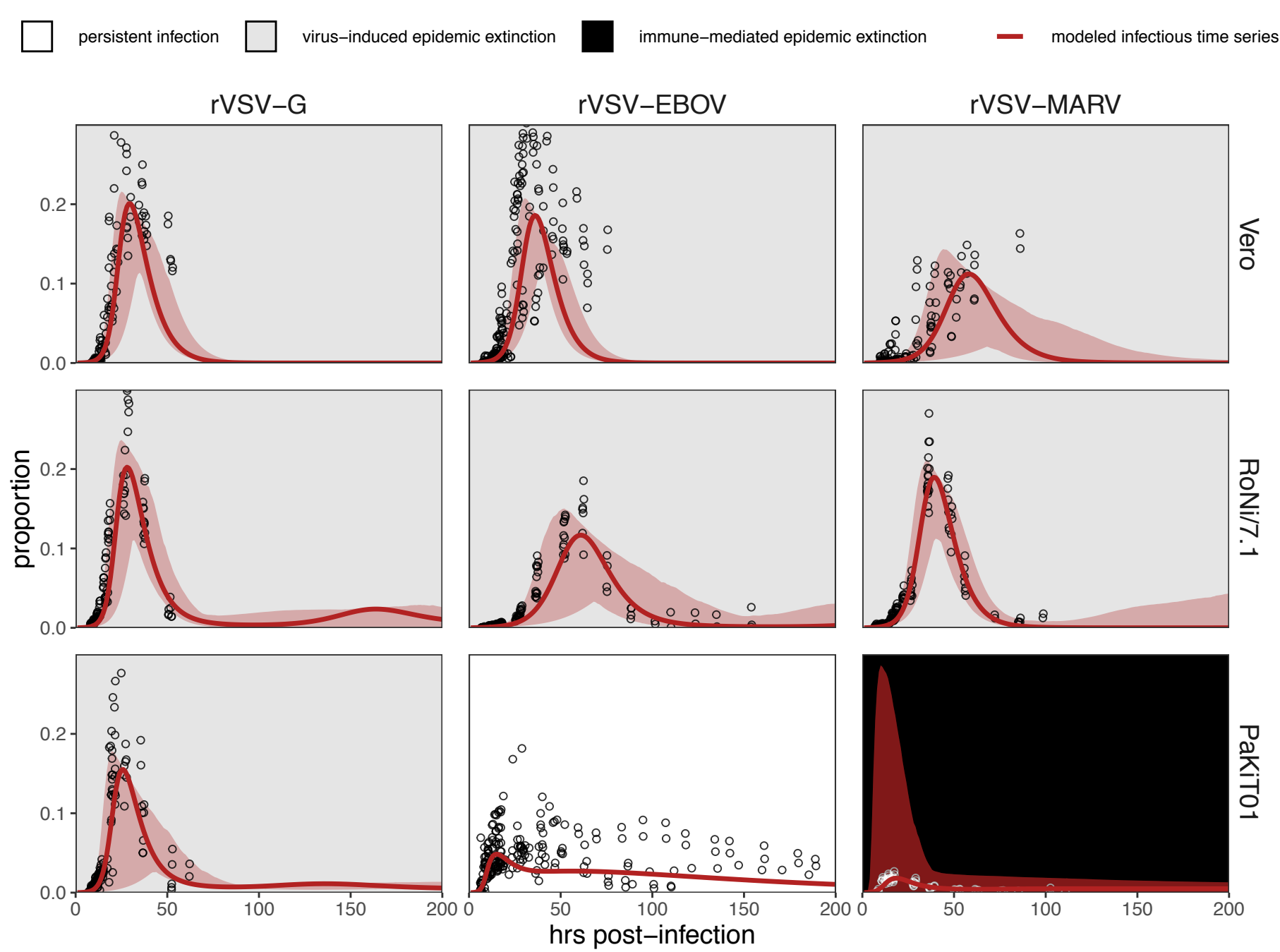
persistent infection
virus−induced epidemic extinction
immune−mediated epidemic extinction
modeled infectious time series
rVSV−G
rVSV−EBOV
rVSV−MARV
Vero
RoNi/7.1
PaKiT01
proportion
0.0
0.1
0.2
0
50
100
150
200
hrs post−infection

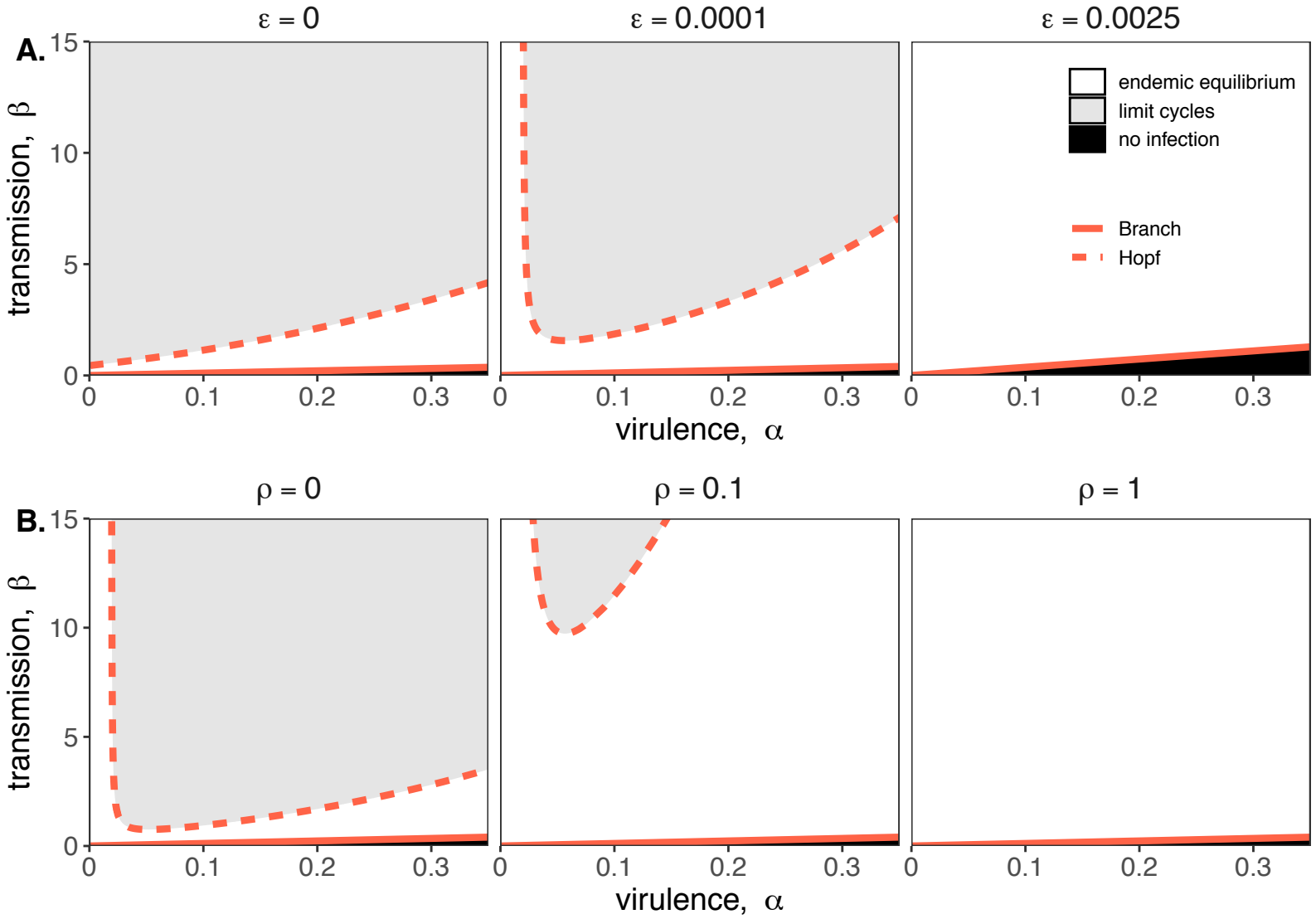
A.
ε = 0
ε = 0.0001
ε = 0.0025
endemic equilibrium
limit cycles
no infection
Branch
Hopf
transmission, β
virulence, α
B.
ρ = 0
ρ = 0.1
ρ = 1
transmission, β
virulence, α

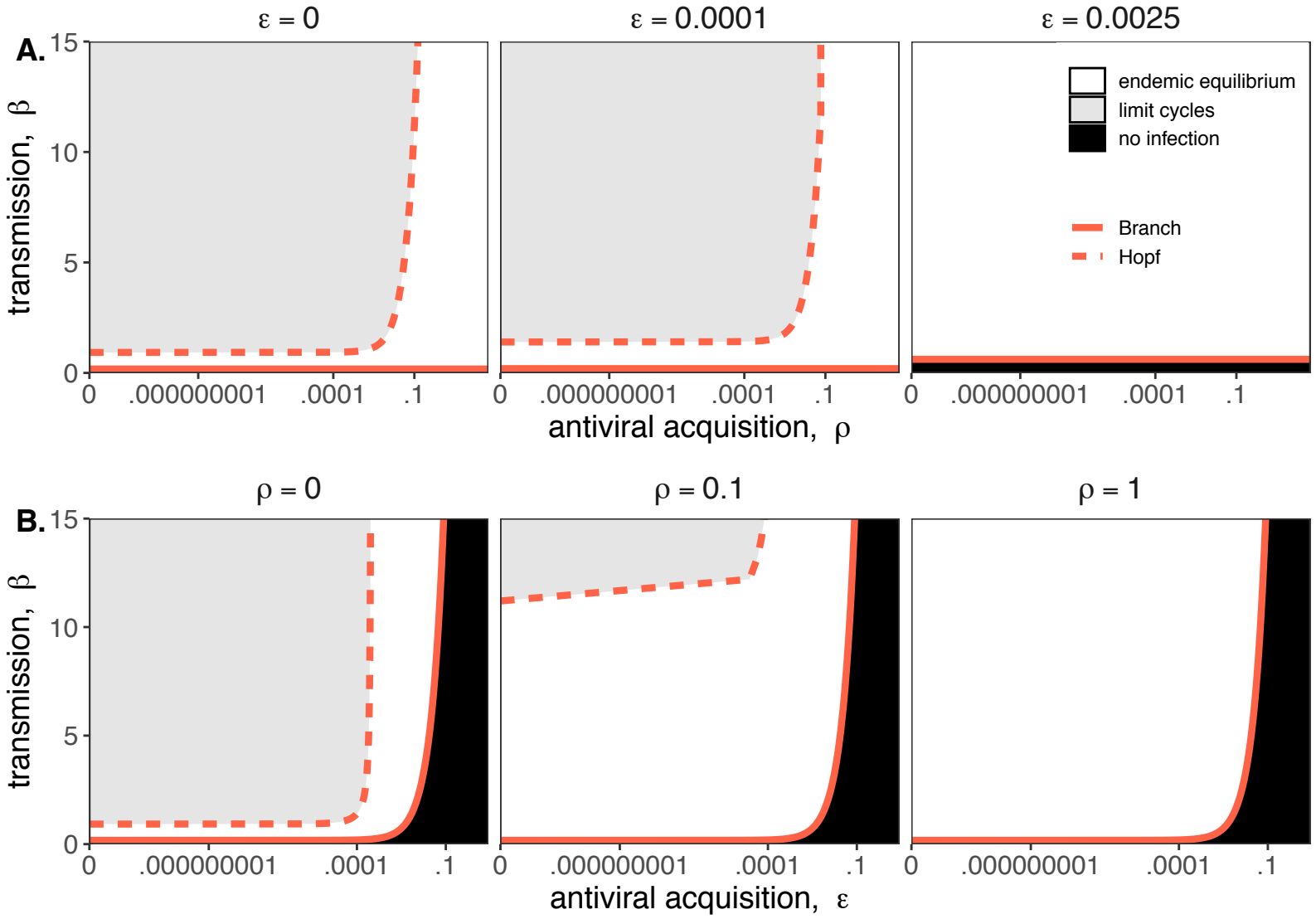
A.
ε = 0
ε = 0.0001
ε = 0.0025
transmission, β
15
10
5
0
0
.000000001
.0001
.1
antiviral acquisition, ρ
endemic equilibrium
limit cycles
no infection
Branch
Hopf
B.
ρ = 0
ρ = 0.1
ρ = 1
antiviral acquisition, ε

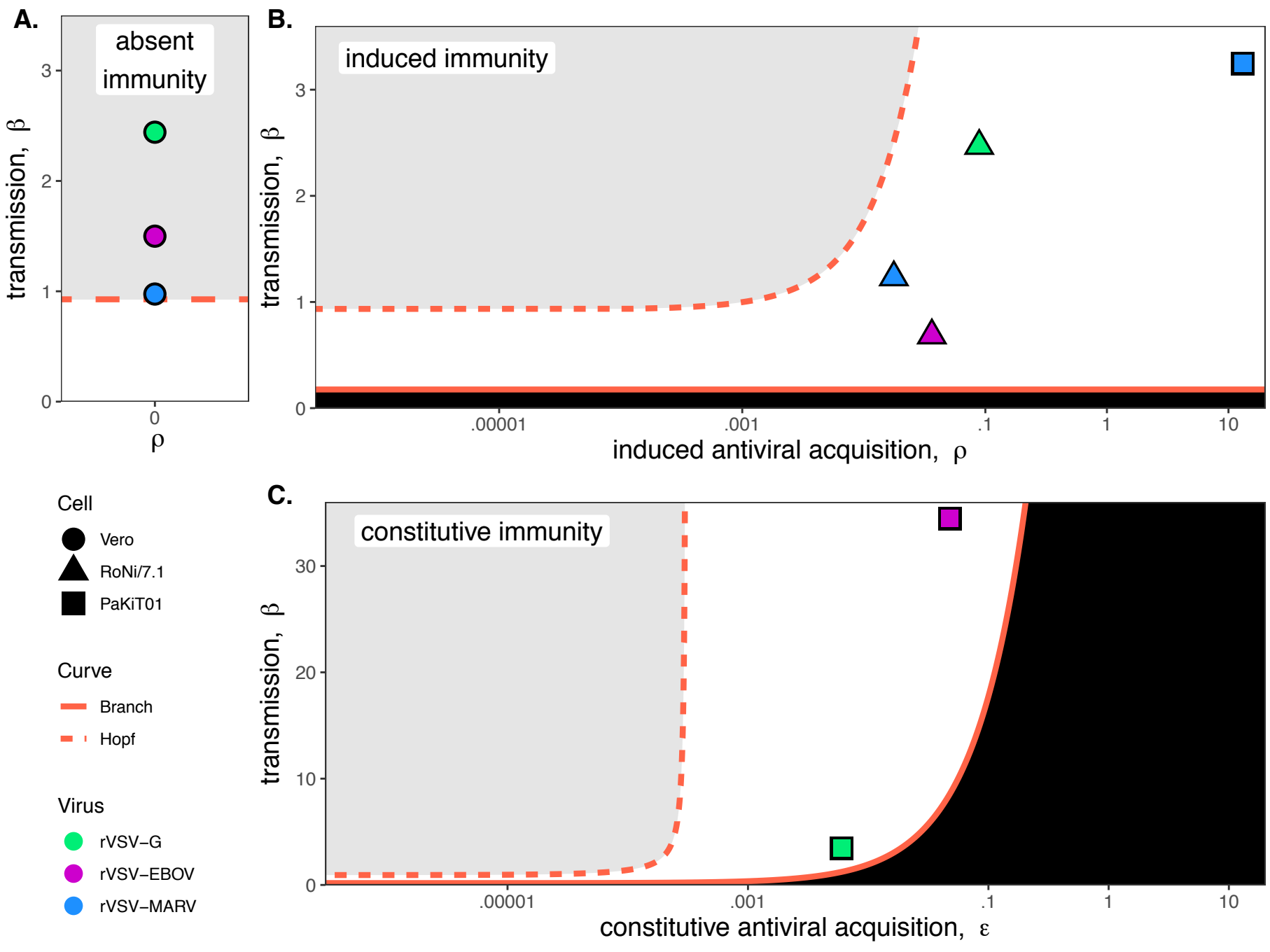
A.
absent immunity
transmission, β
ρ
B.
induced immunity
transmission, β
induced antiviral acquisition, ρ
.00001
.001
.1
1
10
C.
constitutive immunity
transmission, β
constitutive antiviral acquisition, ε
Cell
Vero
RoNi/7.1
PaKiT01
Curve
Branch
Hopf
Virus
rVSV−G
rVSV−EBOV
rVSV−MARV

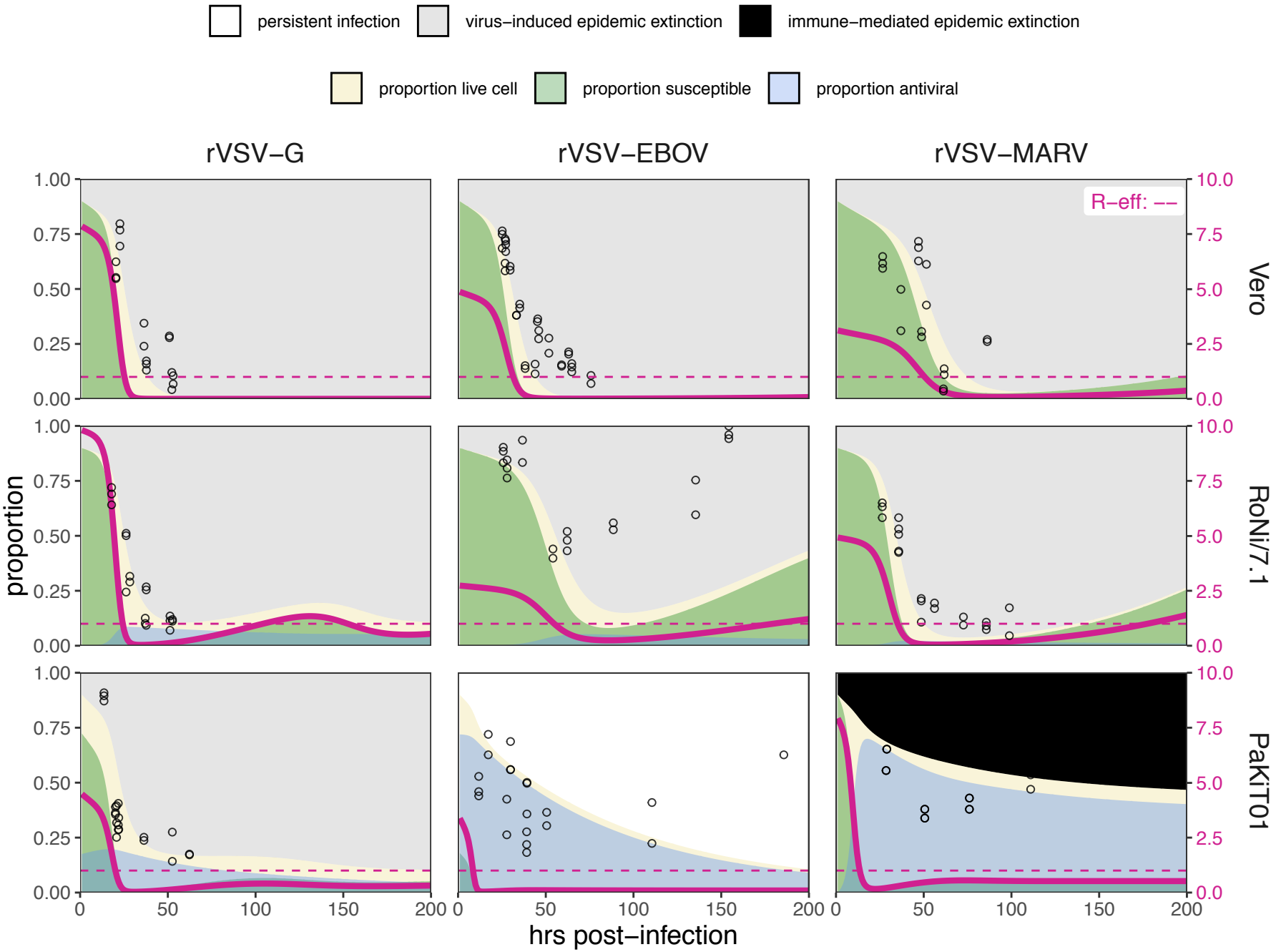
persistent infection
virus−induced epidemic extinction
immune−mediated epidemic extinction
proportion live cell
proportion susceptible
proportion antiviral
rVSV−G
rVSV−EBOV
rVSV−MARV
Vero
RoNi/7.1
PaKiT01
R−eff: −−
proportion
hrs post−infection
1.00
0.75
0.50
0.25
0.00
10.0
7.5
5.0
2.5
0.0
0
50
100
150
200

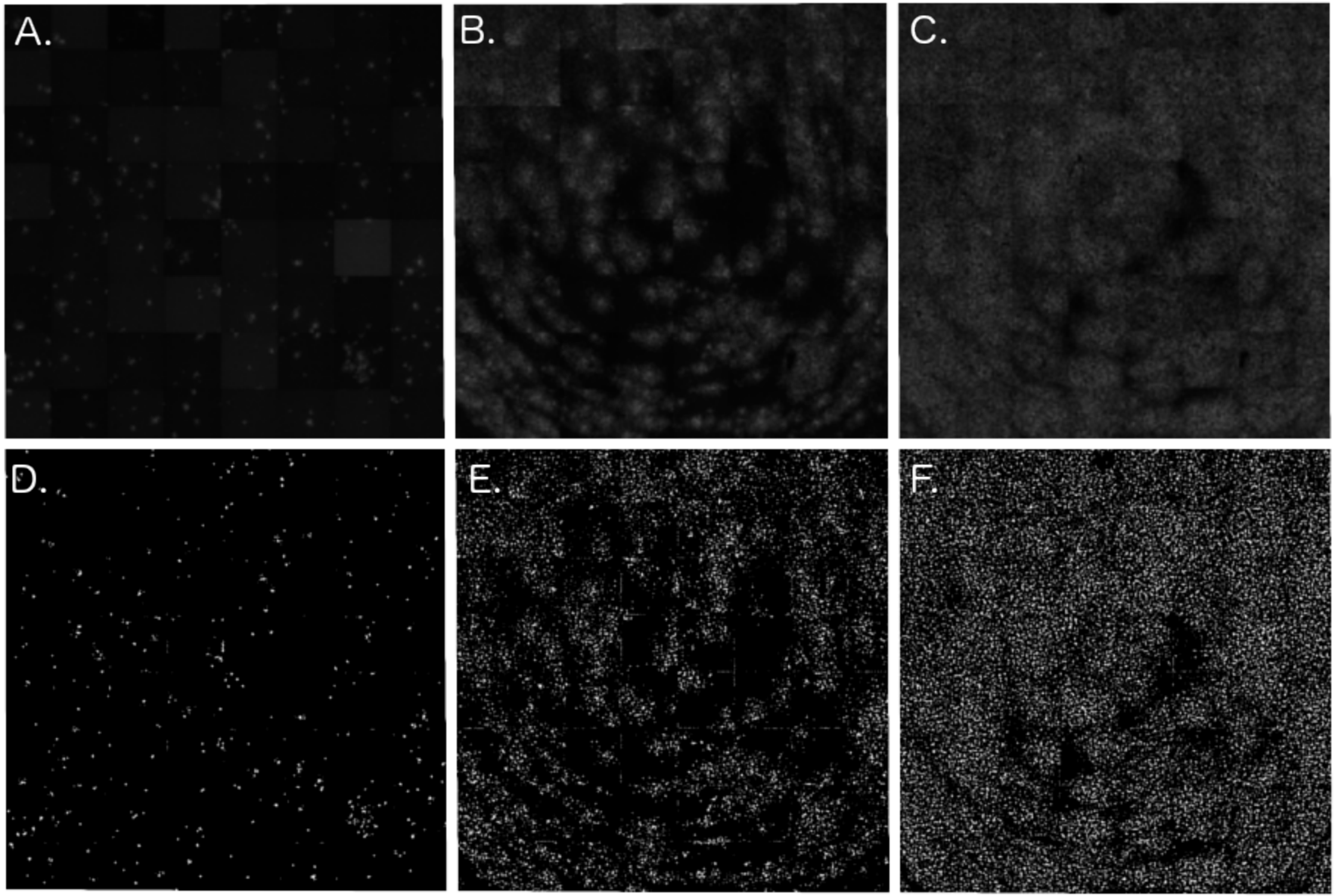
A.
B.
C.
D.
E.
F.

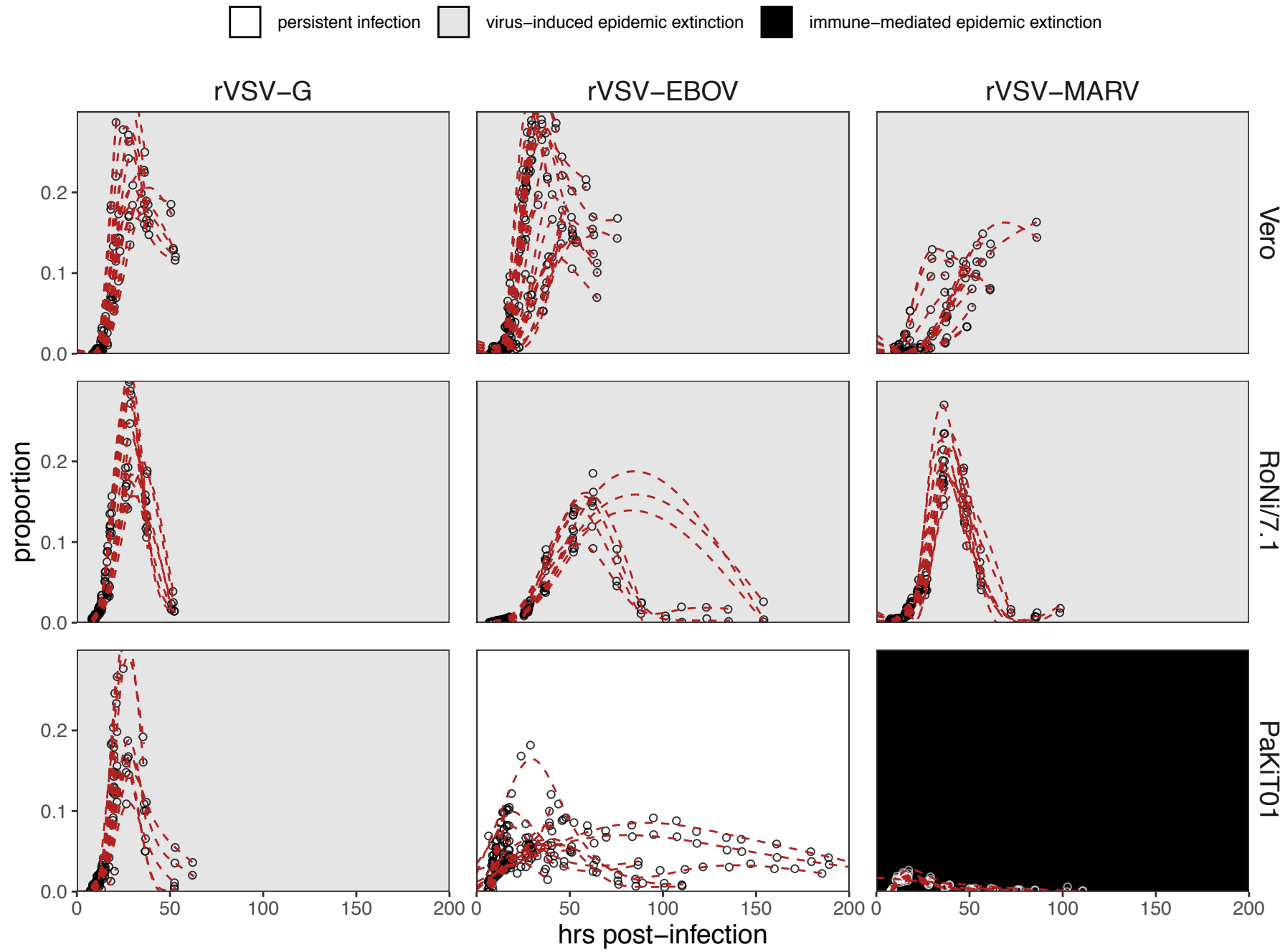
persistent infection
virus−induced epidemic extinction
immune−mediated epidemic extinction
rVSV−G
rVSV−EBOV
rVSV−MARV
Vero
RoNi/7.1
PaKiT01
proportion
0.0
0.1
0.2
0
50
100
150
200
hrs post−infection

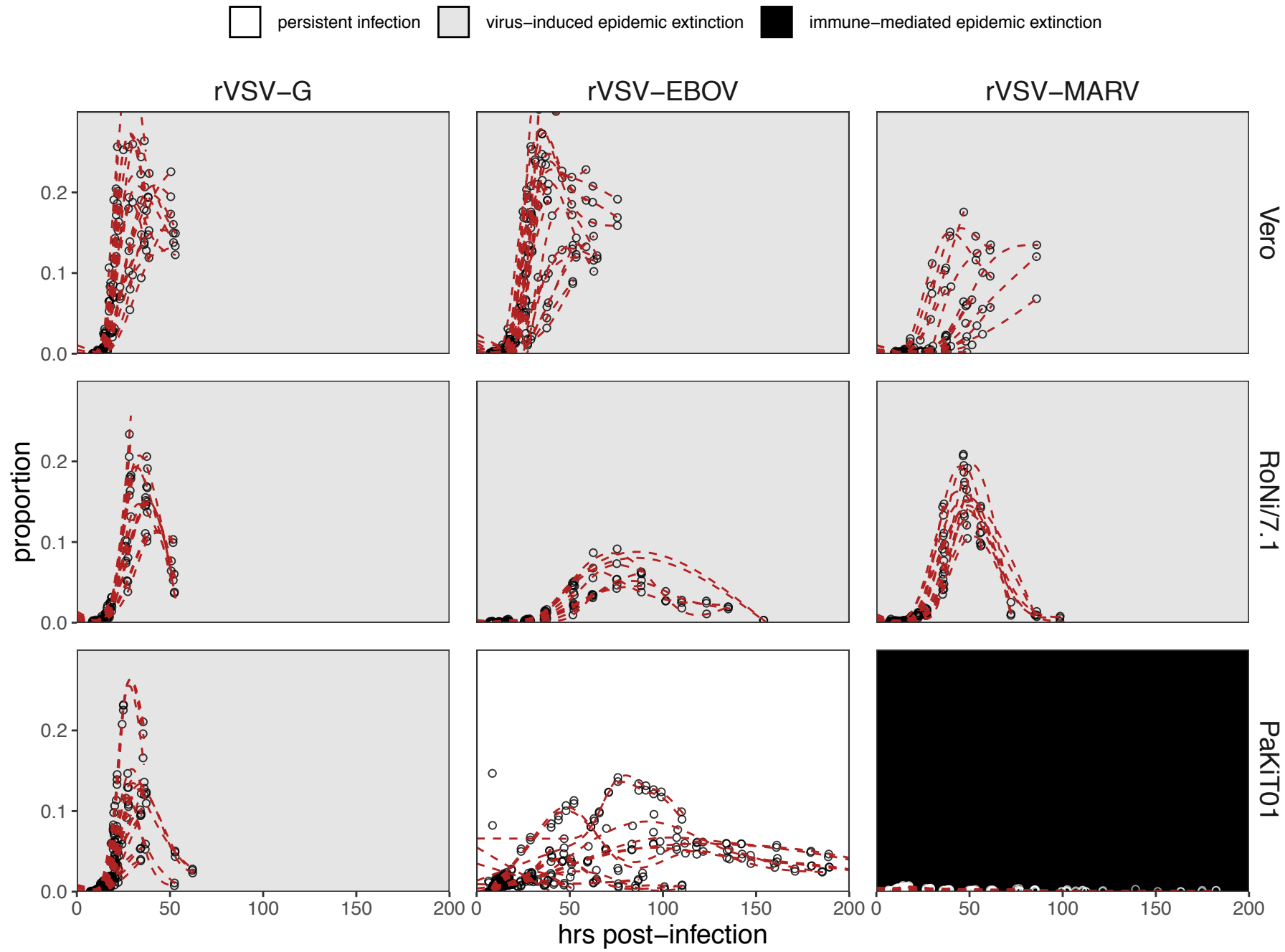
persistent infection
virus−induced epidemic extinction
immune−mediated epidemic extinction
rVSV−G
rVSV−EBOV
rVSV−MARV
Vero
RoNi/7.1
PaKiT01
proportion
0.0
0.1
0.2
0
50
100
150
200
hrs post−infection

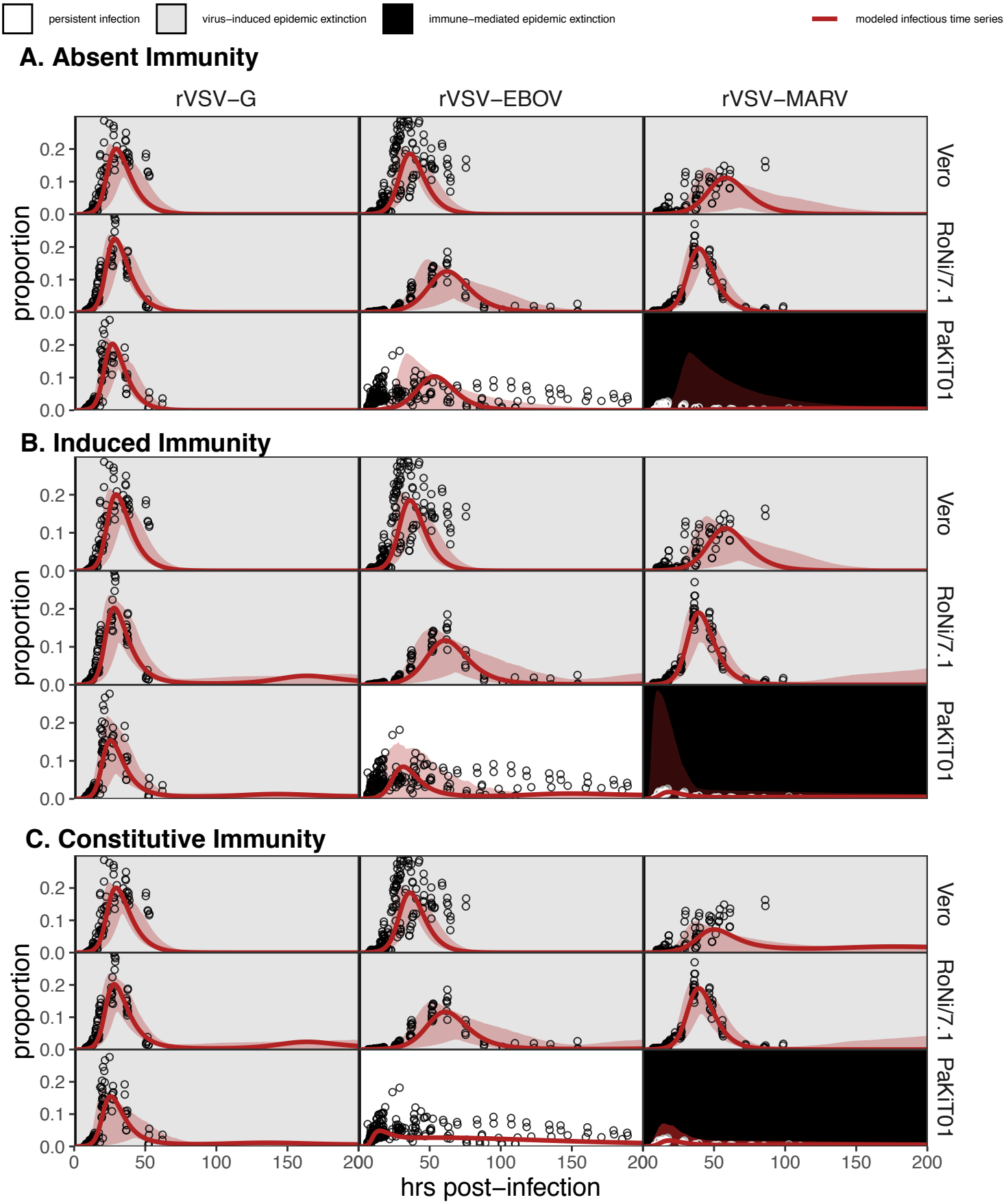
persistent infection
virus−induced epidemic extinction
immune−mediated epidemic extinction
modeled infectious time series
A. Absent Immunity
B. Induced Immunity
C. Constitutive Immunity
rVSV−G
rVSV−EBOV
rVSV−MARV
Vero
RoNi/7.1
PaKiT01
proportion
0.0
0.1
0.2
0
50
100
150
200
hrs post−infection

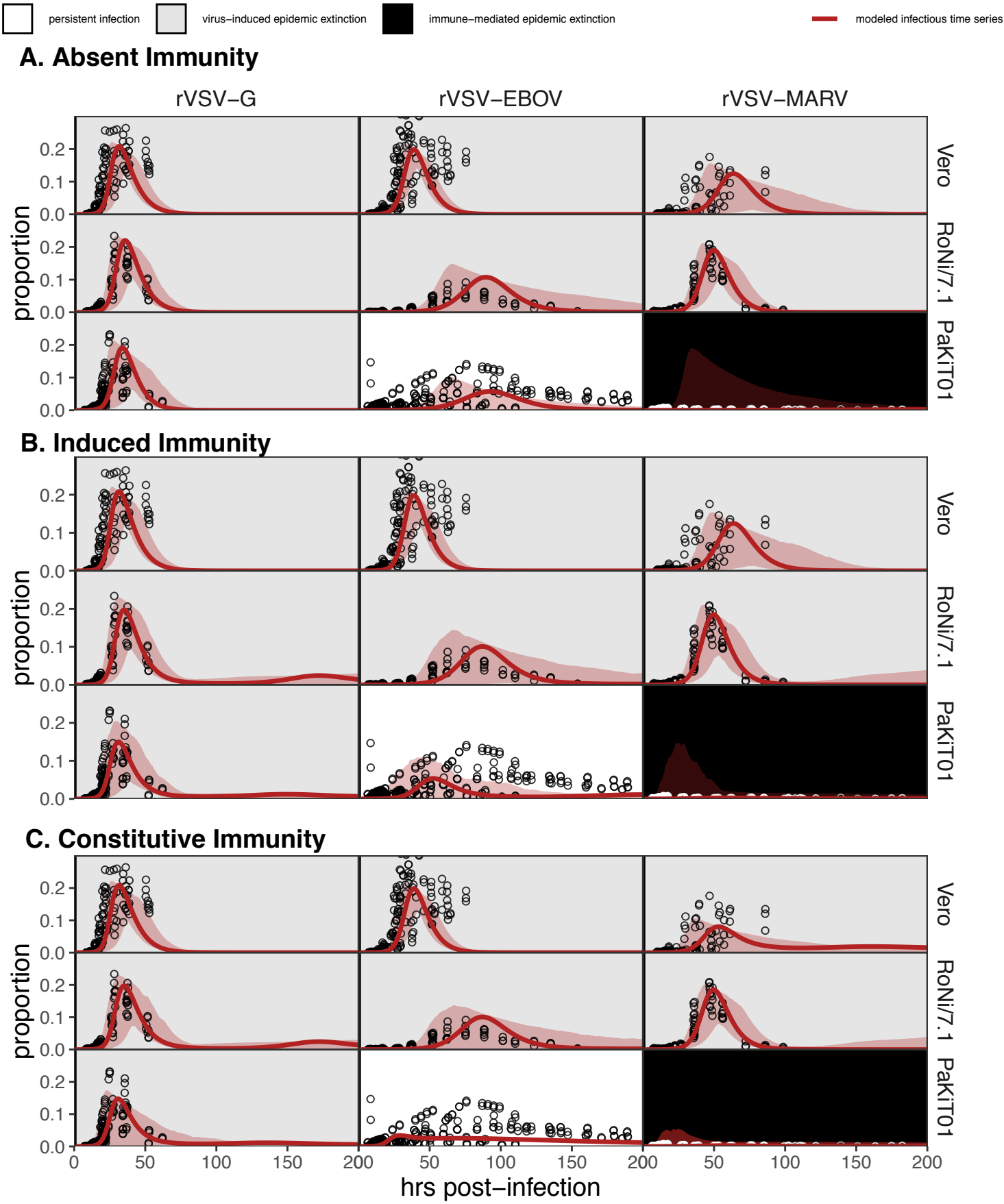
persistent infection
virus−induced epidemic extinction
immune−mediated epidemic extinction
modeled infectious time series
A. Absent Immunity
B. Induced Immunity
C. Constitutive Immunity
rVSV−G
rVSV−EBOV
rVSV−MARV
Vero
RoNi/7.1
PaKiT01
proportion
0.0
0.1
0.2
0
50
100
150
200
hrs post−infection

A. IFN−a

B. IFN−B

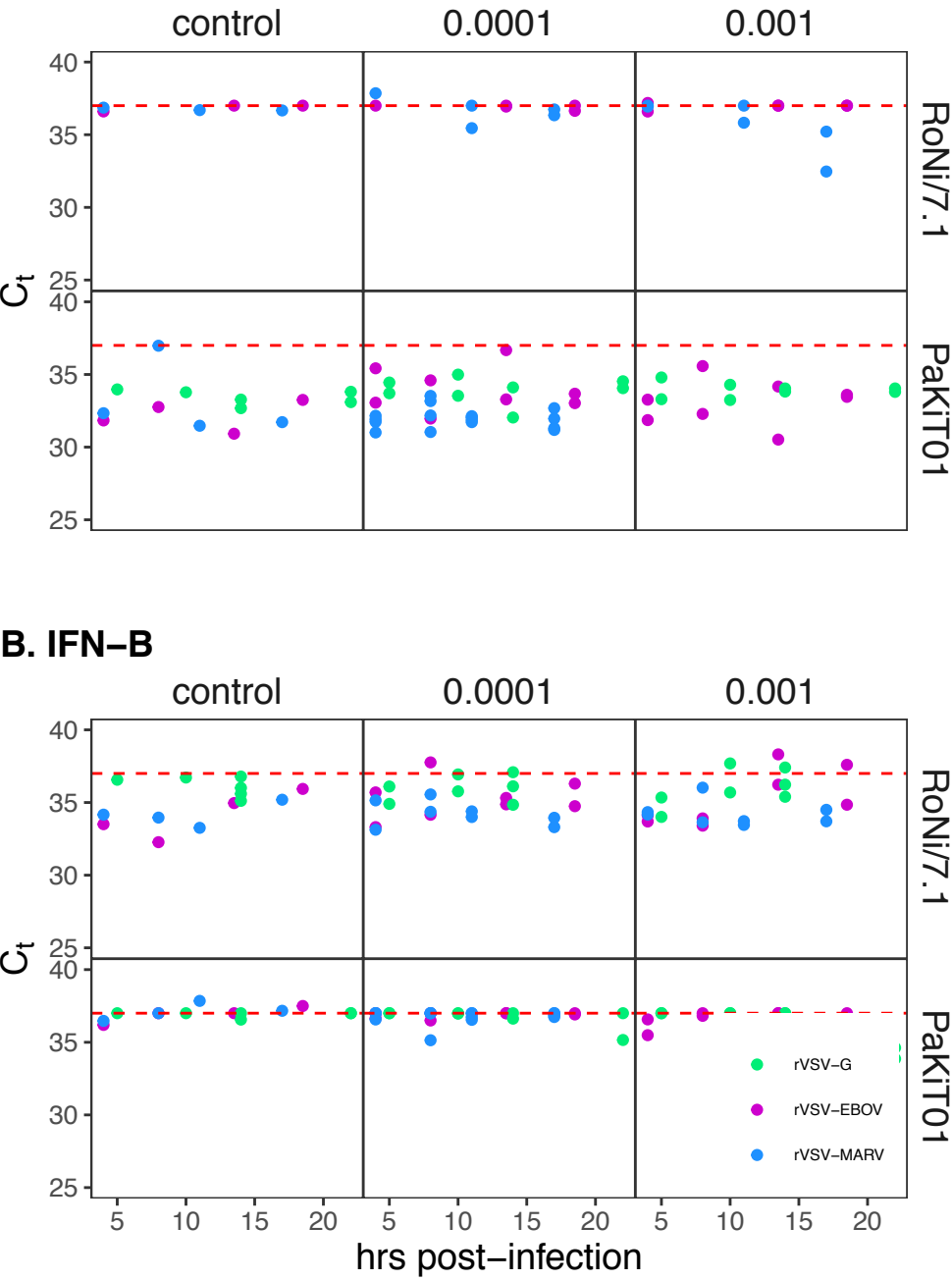
control
0.0001
0.001
RoNi/7.1
PaKiT01
C_t
40
35
30
25
5
10
15
20
hrs post−infection
rVSV−G
rVSV−EBOV
rVSV−MARV

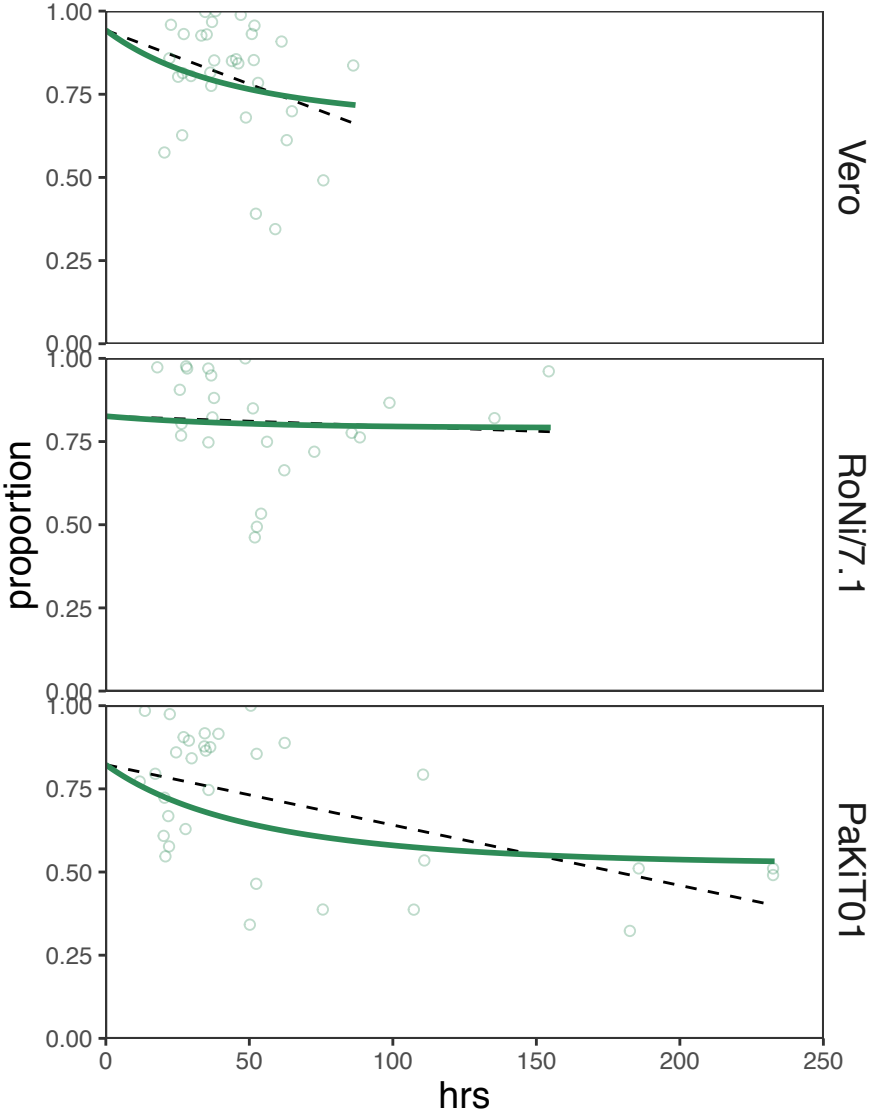
proportion
1.00
0.75
0.50
0.25
0.00
Vero
RoNi/7.1
PaKiT01
0
50
100
150
200
250
hrs

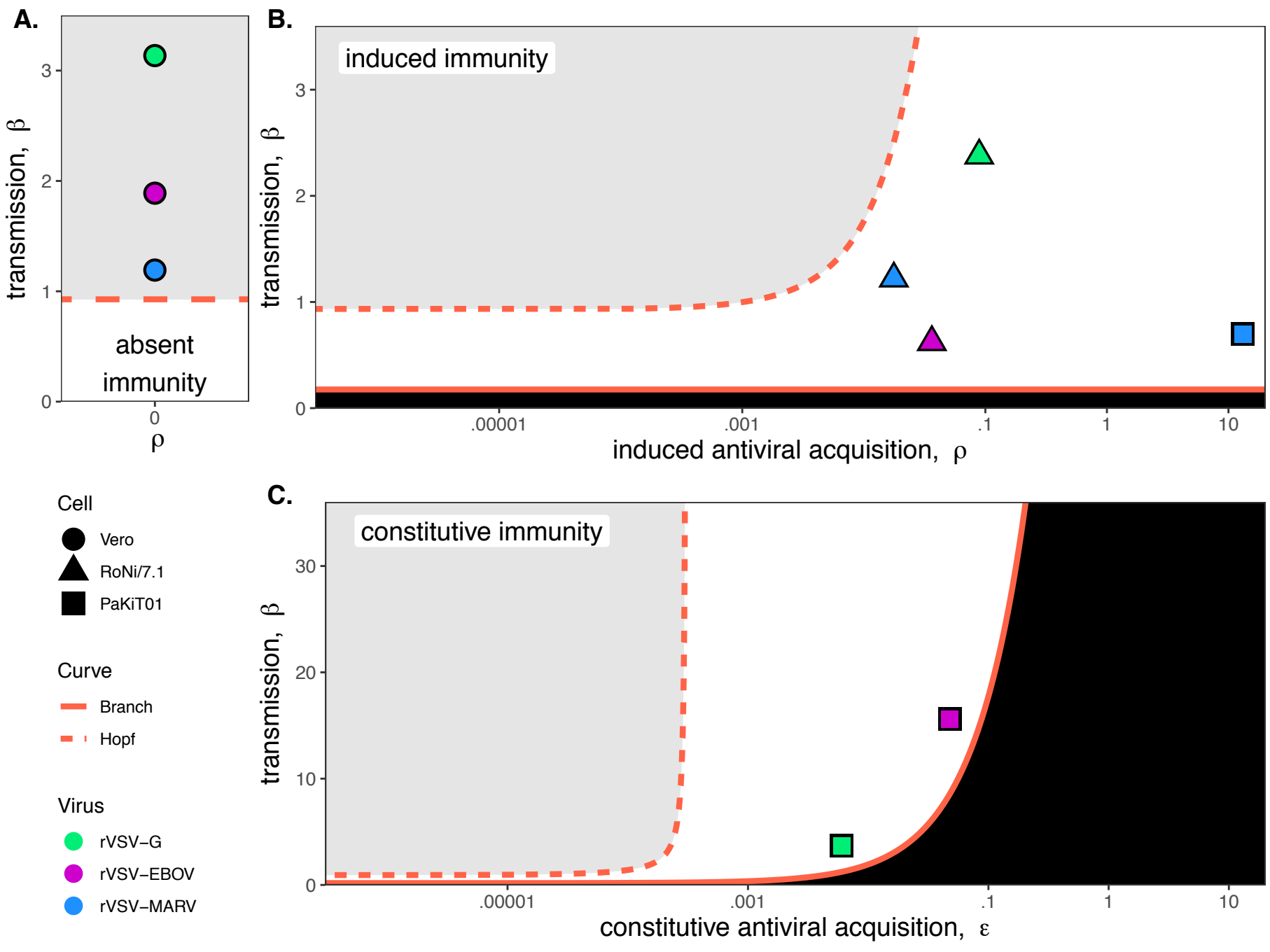
A.
B.
C.
transmission, β
ρ
absent
immunity
induced immunity
induced antiviral acquisition, ρ
constitutive immunity
constitutive antiviral acquisition, ε
Cell
Vero
RoNi/7.1
PaKiT01
Curve
Branch
Hopf
Virus
rVSV−G
rVSV−EBOV
rVSV−MARV

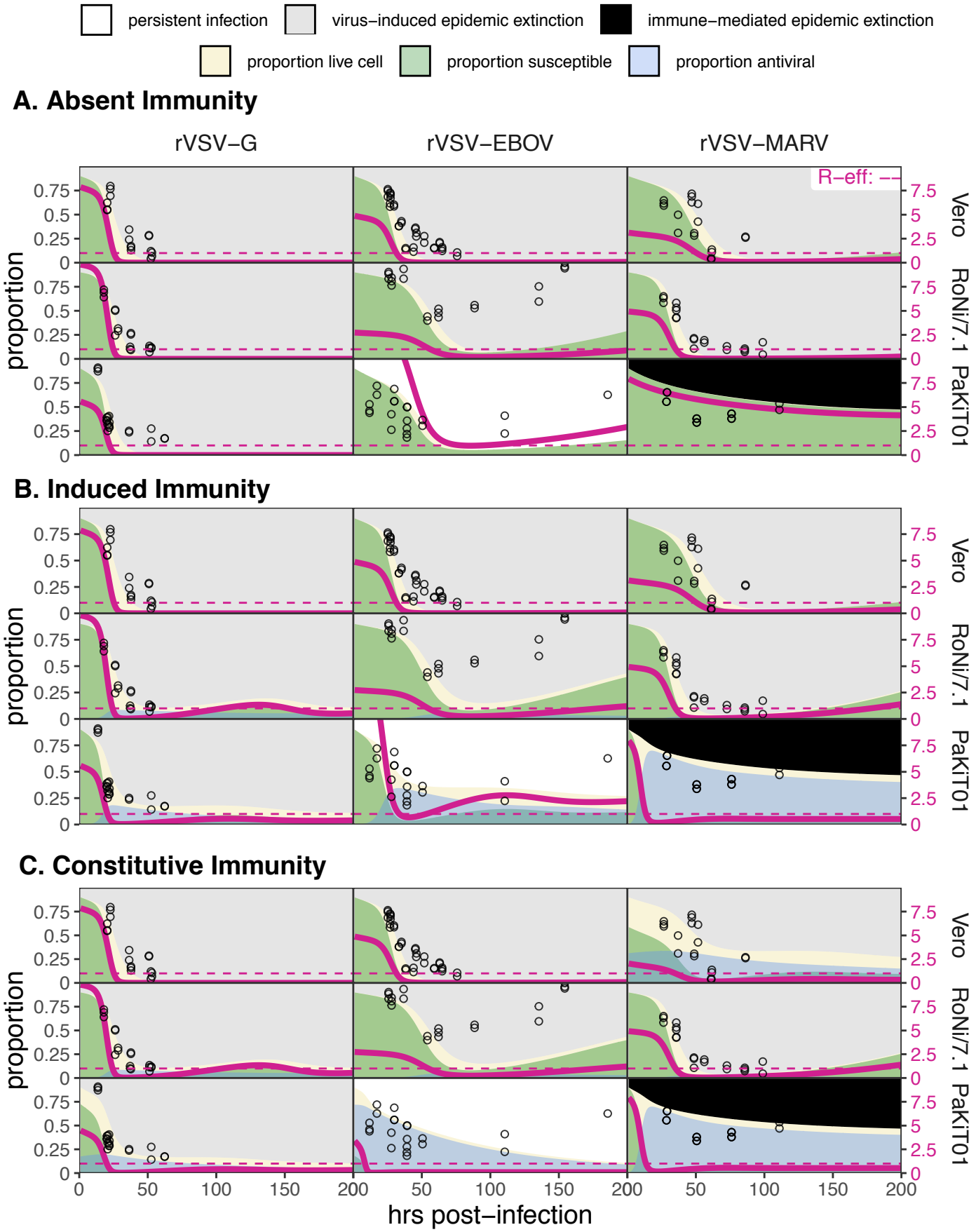
persistent infection
virus−induced epidemic extinction
immune−mediated epidemic extinction
proportion live cell
proportion susceptible
proportion antiviral
A. Absent Immunity
B. Induced Immunity
C. Constitutive Immunity
rVSV−G
rVSV−EBOV
rVSV−MARV
R−eff: −−
Vero
RoNi/7.1
PaKiT01
proportion
hrs post−infection

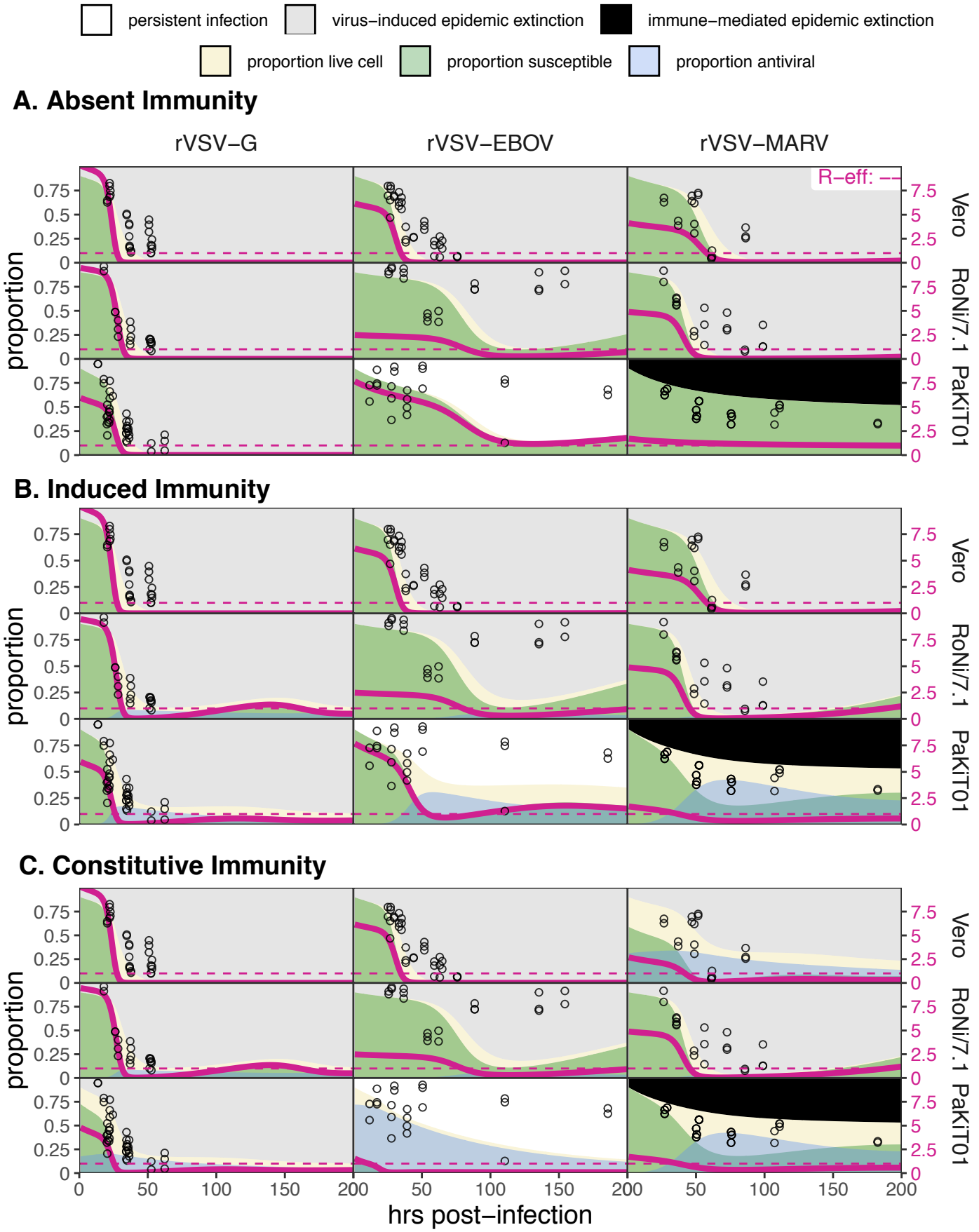
persistent infection
virus−induced epidemic extinction
immune−mediated epidemic extinction
proportion live cell
proportion susceptible
proportion antiviral
A. Absent Immunity
B. Induced Immunity
C. Constitutive Immunity
rVSV−G
rVSV−EBOV
rVSV−MARV
R−eff: −−
Vero
RoNi/7.1
PaKiT01
proportion
hrs post−infection

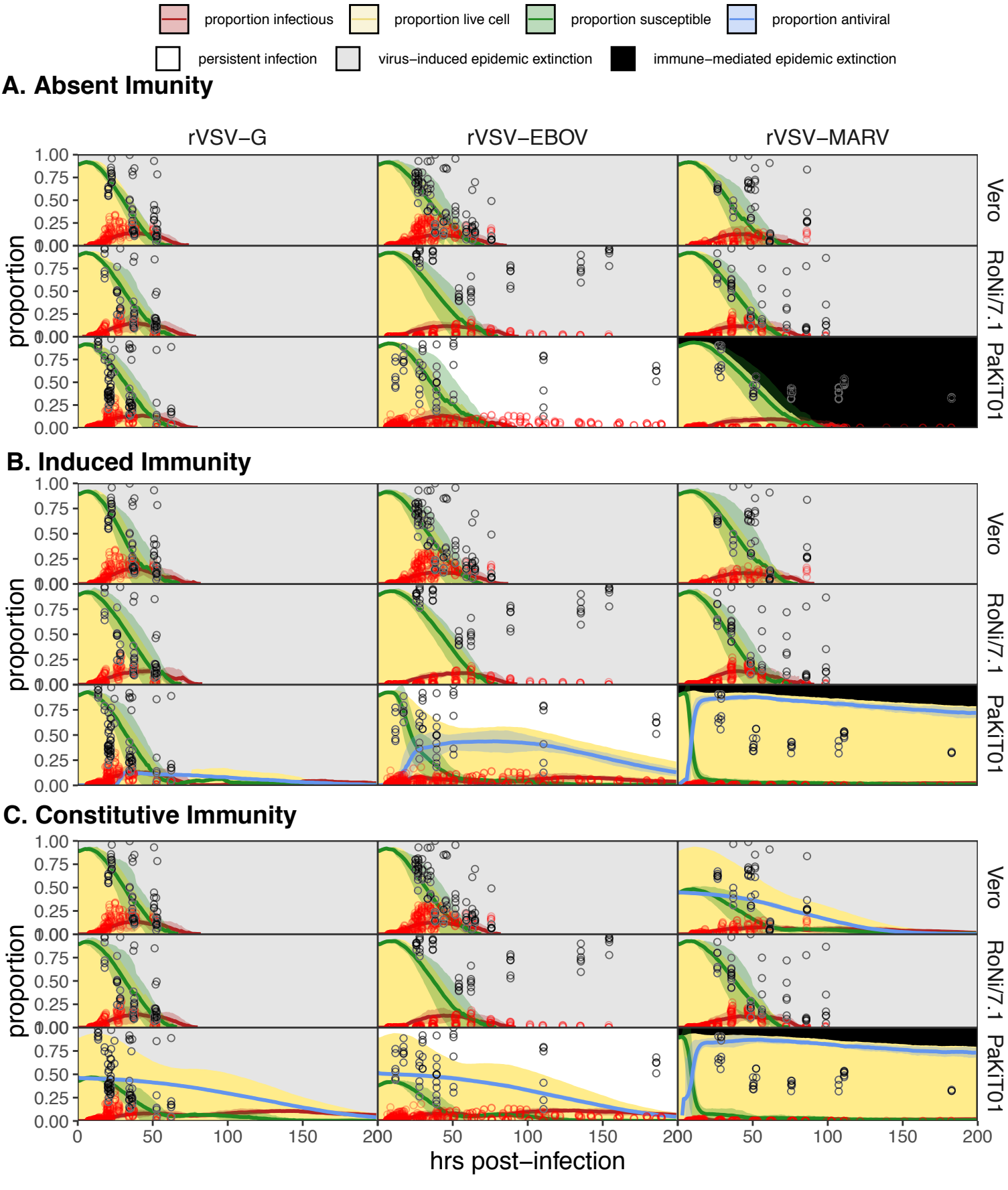
proportion infectious
proportion live cell
proportion susceptible
proportion antiviral
persistent infection
virus−induced epidemic extinction
immune−mediated epidemic extinction
A. Absent Imunity
B. Induced Immunity
C. Constitutive Immunity
rVSV−G
rVSV−EBOV
rVSV−MARV
Vero
RoNi/7.1
PaKiT01
proportion
hrs post−infection
0.00
0.25
0.50
0.75
1.00
0
50
100
150
200

Supplementary File 2. Derivation of R_0

From the main text, we recall that our mean field model takes on the following form:

$$\frac{dP_S}{dt} = bP_D(P_S + P_A) - \beta P_S P_I - \mu P_S - \rho P_E P_S - \varepsilon P_S + cP_A \quad (1)$$

$$\frac{dP_A}{dt} = \rho P_E P_S + \varepsilon P_S - cP_A - \mu P_A \quad (2)$$

$$\frac{dP_E}{dt} = \beta P_S P_I - \sigma P_E - \mu P_E \quad (3)$$

$$\frac{dP_I}{dt} = \sigma P_E - \alpha P_I - \mu P_I \quad (4)$$

$$\frac{dP_D}{dt} = \mu(P_S + P_E + P_I + P_A) + \alpha P_I - bP_D(P_S + P_A) \quad (5)$$

Parameters are defined according to:

- b = natural birth rate; fixed at .025 to yield stable population sizes in *in vitro* models (Figure 1-figure supplement 5)
- μ = natural mortality rate; estimated for each cell line by fitting a simple birth-death model to susceptible declines from control trials; values at $\frac{1}{121}, \frac{1}{191}, \frac{1}{84}$ hours for, respectively, Vero, RoNi/7.1, and PaKiT01 cell lines
- β = transmission coefficient; estimated for each cell line/virus/MOI combination by fitting model to data
- α = infection-induced mortality rate (virulence); fixed at $\frac{1}{6}$ hours
- σ = incubation rate of cell transitioning from an exposed (E) to an infectious (I) state; measured for each cell line-virus combination as the inverse of the time from initial infection to first observation of infectious virus by GFP under the fluorescent micropscope. Respectively, fixed at the following rates: $\frac{1}{8.38}, \frac{1}{7.07}, \frac{1}{9.58}$ hours for rVSV-G, rVSV-EBOV, and rVSV-MARV infections on Vero cells; $\frac{1}{8}, \frac{1}{6.72}, \frac{1}{6.78}$ hours for rVSV-G, rVSV-EBOV, and rVSV-MARV infections on RoNi/7.1 cells; and $\frac{1}{7.17}, \frac{1}{6.03}, \frac{1}{6.42}$ hours for rVSV-G, rVSV-EBOV, and rVSV-MARV infections on PaKiT01 cells
- ρ = rate of infection-induced acquisition to antiviral state, based on the global proportion of exposed cells in the tissue culture; fixed at 0 under conditions of absent immunity and estimated under conditions of induced and constitutive immunity for all cell line/virus combinations by fitting model to joint data over both MOI-0.001 and 0.0001 data.
- ε = rate of constitutive acquisition to antiviral state, based on the global proportion of susceptible cells in the tissue culture; fixed at 0 under assumptions of absent and induced immunity; estimated under conditions of constitutive immunity for all cell line/virus combinations by fitting model to joint data over both MOI=0.001 and 0.0001 data.
- c = rate of return to susceptibility from antiviral status; fixed at 0 in all model fits under all assumptions of immunity. Regression from antiviral status to susceptibility occurs on longer time scales than the 200 hour duration of our cell culture trials
- We assume that $P_S + P_A + P_E + P_I + P_D = 1$

We rewrote the equations to model explicit cell densities within a defined well volume. Note that these two systems of equations are equivalent and that parameter values can be used interchangeably across both forms. In the following system, N indicates the total cell capacity of the area modeled:

$$\frac{dS}{dt} = bD\frac{(S+A)}{N} - \frac{\beta SI}{N} - \mu S - \frac{\rho ES}{N} - \varepsilon S + cA \quad (6)$$

$$\frac{dA}{dt} = \frac{\rho ES}{N} + \varepsilon S - cA - \mu A \quad (7)$$

$$\frac{dE}{dt} = \frac{\beta SI}{N} - \sigma E - \mu E \quad (8)$$

$$\frac{dI}{dt} = \sigma E - \alpha I - \mu I \quad (9)$$

$$\frac{dD}{dt} = \mu(S + E + I + A) + \alpha I - bD\frac{(S+A)}{N} \quad (10)$$

To solve for R_0, we adopted a next generation matrix approach, after Heffernan, Smith, and Wahl 2005, which we applied to the proportional system of equations (1-5, above). Step one of this process necessitated constructing two transition matrices: the F matrix, which describes how new infections are created and the V matrix which represents host transitions between exposed and infected states.

To build these F and V matrices, we first calculated the value of P_S at the disease free equilibrium (DFE, whereby P_I and P_E are equal to zero. We allow for the presence of antiviral cells (P_A) at disease free equilibrium, though their equilibrium quantity (and, by consequence, the extent of constitutive immunity at play in the system) depends on certain parameter values. When $\varepsilon = 0$, P_A will always be 0 at disease free equilibrium. By allowing the extent of constitutive immunity to vary with parameter values, we maintain consistency with the published literature, which suggests that, in constitutively antiviral bat cell lines (i.e. PaKiT01), some interferon-stimulated genes (ISGs) are perpetually expressed, like their IFN-α precursor, while others still require induction upon infection. At DFE, our antiviral population takes on the following form:

$$P_A^* = \frac{\varepsilon P_S}{(c+\mu)} \quad (11)$$

And, by extension, our susceptible population can be represented as:

$$P_S^* = \frac{(b-\mu)(c+\mu)}{b(c+\mu+\varepsilon)} \quad (12)$$

For cells with either absent or fully induced immunity, for which $\varepsilon = 0$, this contracts to:

$$P_S^* = \frac{(b-\mu)}{b} \quad (13)$$

Because we cannot have negative cell proportions at equilibrium, we impose the following constraint on the above parameters:

$$(b-\mu)(c+\mu) > 0 \tag{14}$$

When we substitute the above value for P_S* into the infectious equations, we find:

$$\frac{dP_E}{dt} = 0 = \frac{\beta(b-\mu)(c+\mu)}{b(c+\mu+\varepsilon)} P_I - \sigma P_E - \mu P_E \tag{15}$$

$$\frac{dP_I}{dt} = 0 = \sigma P_E - \alpha P_I - \mu P_I \tag{16}$$

Our F matrix then takes on the following form:

$$F = \begin{bmatrix} 0 & \frac{\beta(b-\mu)(c+\mu)}{b(c+\mu+\varepsilon)} \\ 0 & 0 \end{bmatrix} \tag{17}$$

And the V matrix takes on the following form:

$$V = \begin{bmatrix} -(\sigma+\mu) & 0 \\ \sigma & -(\alpha+\mu) \end{bmatrix} \tag{18}$$

After Heffernan, Smith, and Wahl 2005, it follows that $G = -FV^{-1}$. Thus, it follows that:

$$V^{-1} = \begin{bmatrix} \frac{1}{(\sigma+\mu)} & 0 \\ \frac{\sigma}{(\sigma+\mu)(\alpha+\mu)} & \frac{1}{(\alpha+\mu)} \end{bmatrix} \tag{19}$$

When this F matrix is multiplied by matrix $-V^{-1}$, we find:

$$G = \begin{bmatrix} \frac{\beta\sigma(b-\mu)(c+\mu)}{b(\sigma+\mu)(\alpha+\mu)(c+\mu+\varepsilon)} & \frac{\beta(b-\mu)(c+\mu)}{b(\alpha+\mu)(c+\mu+\varepsilon)} \\ 0 & 0 \end{bmatrix} \tag{20}$$

which, after matrix algebra, yields the following equation for R_0:

$$R_0 = \frac{\beta\sigma(b-\mu)(c+\mu)}{b(\sigma+\mu)(\alpha+\mu)(c+\mu+\varepsilon)} \tag{21}$$

Pathogens can invade a host tissue under conditions of $R_0 > 1$, or when the system satisfies the following inequality:

$$\beta\sigma(b-\mu)(c+\mu) > b(\sigma+\mu)(\alpha+\mu)(c+\mu+\varepsilon) \tag{22}$$

Finally, we note that for all cells lacking in constitutive antiviral properties ($\varepsilon = 0$), R_0 reduces to:

$$R_0 = \frac{\beta\sigma(b-\mu)}{b(\alpha+\mu)(\sigma+\mu)} \tag{23}$$

Supplementary File 3. Special Points from Bifurcation Analysis

Special Point	**ε**	**ρ**	**β**	**P_I**
Branch Point	0	.01	0.176	0
Hopf	0	.01	1.76	0.0133
Branch Point	0.0001	.01	0.193	0
Hopf	0.0001	.01	2.747	0.00944
Branch Point†	0.0025	.01	0.615	0
Branch Point	0.0001	0	0.193	0
Hopf	0.0001	0	1.407	0.0156
Branch Point	0.0001	.1	0.193	0
Hopf	0.0001	.1	16.918	0.00178
Branch Point†	0.0001	1	0.193	0

Note: All other parameters in this bifurcation analysis were fixed at the following values: b =.025 ; $\mu = 0.001$; $\sigma = \frac{1}{6}$; $\alpha = \frac{1}{6}$; $c = 0$

†For these scenarios with high antiviral rates (either induced, ρ, or constitutive, ε), no Hopf bifurcation was observed.

Supplementary File 4. Optimized parameters from all deterministic model outputs and spatial approximations

Assumption	Cell Line	Virus	δ AIC†	ε [lci – uci] *	ρ [lci – uci] *	MOI	Antiviral Rate	β [lci – uci] *	Mean Field R_0	Spatial β
Absent	Vero	rVSV-G	0	0	0 [0-0]	0.0001	0	3.14 [1.86-4.41]	11.211	--
						0.001	0	2.44 [1.52-3.36]	8.729	24.418
		rVSV-EBOV	0	0	0 [0-0]	0.0001	0	1.89 [1.42-2.36]	6.823	--
						0.001	0	1.5 [1.06-1.94]	5.416	14.996
		rVSV-MARV	0	0	0 [0-0]	0.0001	0	1.19 [0.624-1.76]	4.223	--
						0.001	0	0.975 [0.558-1.39]	3.454	9.752
	RoNi/7.1	rVSV-G	32.7	0	0 [0-0]	0.0001	0	2.33 [1.39-3.27]	10.278	--
						0.001	0	2.42 [1.54-3.3]	10.686	24.205
		rVSV-EBOV	222	0	0 [0-0]	0.0001	0	0.609 [.367-0.851]	2.707	--
						0.001	0	0.675 [.466-0.885]	3.001	6.753
		rVSV-MARV	3.36	0	0 [0-0]	0.0001	0	1.22 [0.891-1.54]	5.405	--
						0.001	0	1.23 [0.924-1.53]	5.457	12.284
	PaKiT01	rVSV-G	175	0	0 [0-0]	0.0001	0	2.48 [1.38-3.58]	6.689	--
						0.001	0	2.56 [1.58-3.55]	6.917	25.639
		rVSV-EBOV	27.9	0	0 [0-0]	0.0001	0	0.663 [.399-0.927]	1.811	--
						0.001	0	0.837 [0.215-1.46]	2.287	8.37
		rVSV-MARV	665	0	0 [0-0]	0.0001	0	0.393 [0-2.2]	1.068	--
						0.001	0	0.379 [0-1.66]	1.03	3.785
Induced	Vero	rVSV-G	2	0 [0-0]	4.55×10^{-10} [0-3.92×10^{-7}]	0.0001	3.04×10^{-14}	3.14 [1.86-4.41]	11.211	--
						0.001	3.04×10^{-13}	2.44 [1.52-3.36]	8.727	24.413
		rVSV-EBOV	2	0 [0-0]	4.64×10^{-8} [0-4.38×10^{-7}]	0.0001	3.11×10^{-12}	1.89 [1.42-2.36]	6.824	--
						0.001	3.10×10^{-11}	1.5 [1.06-1.94]	5.416	14.996
		rVSV-MARV	2	0 [0-0]	2.05×10^{-7} [0-5.97×10^{-7}]	0.0001	1.37×10^{-11}	1.19 [0.624-1.76]	4.223	--
						0.001	1.37×10^{-10}	0.975 [0.558-1.39]	3.454	9.752
	RoNi/7.1	rVSV-G	0	0 [0-0]	0.089 [0-0.432]	0.0001	7.03×10^{-6}	2.38 [1.37-3.39]	10.504	--
						0.001	7.03×10^{-5}	2.47 [1.49-3.45]	10.907	24.705
		rVSV-EBOV	0	0 [0-0]	0.0363 [0-0.343]	0.0001	2.87×10^{-6}	.622 [.336-.907]	2.763	--
						0.001	2.87×10^{-5}	.685 [.451-.919]	3.043	6.849
		rVSV-MARV	0	0 [0-0]	0.0177 [0-0.257]	0.0001	1.40×10^{-6}	1.22 [.882-1.56]	5.424	--
						0.001	1.40×10^{-5}	1.23 [.917-1.55]	5.475	12.324
	PaKiT01	rVSV-G	29.9	0 [0-0]	0.311 [0-1.02]	0.0001	1.63×10^{-5}	2.8 [1.43-4.17]	7.562	--
						0.001	0.000162	2.72 [1.4-4.03]	7.334	27.183
		rVSV-EBOV	1020	0 [0-0]	0.881 [0-3.32]	0.0001	0.0000461	1.08 [0-2.65]	2.947	--
						0.001	0.000461	1.55 [0-4.08]	4.233	15.495
		rVSV-MARV	0	0 [0-0]	13.1 [0-37.9]	0.0001	0.000687	0.698 [0-10.1]	1.9	--
						0.001	0.00687	3.25 [0-41.3]	8.828	32.452

Constitutive	Vero	rVSV-G	4	2.86×10^{-24} [0-0.00237]	3.05×10^{-8} [0-0.00237]	0.0001	2.04×10^{-12}	3.14 [1.81-4.47]	11.211	--
						0.001	2.04×10^{-11}	2.44 [1.49-3.4]	8.73	24.42
		rVSV-EBOV	4	5.42×10^{-20} [0-0.00202]	2.39×10^{-8} [0-0.00202]	0.0001	1.60×10^{-12}	1.89 [1.39-2.39]	6.824	--
						0.001	1.60×10^{-11}	1.5 [1.03-1.97]	5.416	14.996
		rVSV-MARV	247	0.00725 [0.00325-0.0113]	4.84×10^{-10} [0-3.92×10^{-7}]	0.0001	0.00259	2.42 [0.672-4.16]	4.565	--
						0.001	0.00259	1.83 [0.626-3.04]	3.464	18.347
	RoNi/7.1	rVSV-G	2	6.14×10^{-10} [0-3.93×10^{-7}]	0.089 [0-0.432]	0.0001	7.03×10^{-6}	2.38 [1.37-3.39]	10.504	--
						0.001	7.03×10^{-5}	2.47 [1.49-3.45]	10.906	24.703
		rVSV-EBOV	2.01	1.08×10^{-9} [0-3.93×10^{-7}]	0.0366 [0-0.346]	0.0001	2.90×10^{-6}	0.622 [0.336-0.908]	2.763	--
						0.001	2.89×10^{-5}	0.685 [0.45-0.919]	3.042	6.846
		rVSV-MARV	2	5.54×10^{-10} [0-3.93×10^{-7}]	0.0176 [0-0.257]	0.0001	1.40×10^{-6}	1.22 [0.882-1.56]	5.424	--
						0.001	1.39×10^{-5}	1.23 [0.917-1.55]	5.475	12.324
	PaKiT01	rVSV-G	0	0.00602 [0-0.019]	8.26×10^{-8} [0-4.75×10^{-7}]	0.0001	0.00209	3.68 [0.919-6.44]	6.593	--
						0.001	0.00209	3.45 [1.07-5.84]	6.189	34.516
		rVSV-EBOV	0	0.0478 [0-0.0958]	4.46×10^{-8} [0-4.37×10^{-7}]	0.0001	0.00499	15.6 [12.7-18.5]	8.518	--
						0.001	0.00499	34.5 [28.7-40.2]	18.823	344.821
		rVSV-MARV	2	3.99×10^{-7} [6.86×10^{-9}-7.91×10^{-7}]	13.1 [1.48-24.8]	0.0001	0.000687	0.699 [0-10.1]	1.902	--
						0.001	0.00687	3.24 [0-14.5]	8.815	32.406

†Best fit models indicated at δ-AIC = 0 are presented in Table 1 and Figure 1 and 3 (main text)

* lci = lower and uci = upper 95% confidence interval. No confidence interval is shown for spatial β which was fixed at 10 times the estimated mean for the mean field model fits when paired with equivalent values of ε and ρ.

All other parameters were fixed at the following values: b=.025 (mean field), .15 (spatial); $\alpha = 1/6$; c=0; $\mu = 1/121$ (Vero), 1/191(RoNi/7.1, and 1/84 (PaKiT01)

Supplementary File 5. Justification for parameter increase from mean field to spatial model.

Because spatial configurations elevate thresholds for pathogen invasion, as well for host cell persistence (Webb, Keeling, and Boots 2007), we were forced to elevate both birth rates (b) and transmission rates (β) above those used in the mean field model to apply to the spatial context. We here justify our chosen values for parameter increase:

In Webb, Keeling, and Boots 2007, the authors approximate spatial dynamics using a series of differential equations tracking the pairwise neighbor-neighbor interactions of a regular square lattice with a Von Neumann neighborhood. Webb *et al.* represent local reproduction as $b(1 - L_b)/z$ and local transmission as $\beta(1 - L_I)/z$ where z is the number of near-neighbor pairs, L_b is the proportion of global reproduction (births), and L_I is the proportion of global transmission in the system. Note that we altered the reproduction parameter *r* to *b* to reflect our own nomenclature.

Cumulatively, we can represent total reproduction (b) and total transmission (β_{tot}) in a system with both local and global effects as:

$$b_{tot} = \frac{b(1-L_b)}{z} + bL_b \tag{1}$$

$$\beta_{tot} = \frac{\beta(1-L_I)}{z} + \beta L_I \tag{2}$$

Our goal is to find a scalar (q) by which to multiply the mean field birth (q_b) and transmission (q_β) rates to values appropriate for the spatial context, such that:

$$b_{spatial} = q_b b_{mean} \tag{3}$$

$$\beta_{spatial} = q_\beta \beta_{mean} \tag{4}$$

Since we know that L_b and L_I both equal 1 in the mean field model, we can represent these interactions as:

$$b_{mean} = \frac{q_b b_{mean}(1-L_b)}{z} + q_b b_{mean} L_b \tag{5}$$

$$\beta_{mean} = \frac{q_\beta \beta_{mean}(1-L_b)}{z} + q_\beta \beta_{mean} L_b \tag{6}$$

And then solve for (q_b) and (q_β):

$$q_b = \frac{z}{zL_b + 1 - L_b} \tag{7}$$

$$q_\beta = \frac{z}{zL_I + 1 - L_I} \tag{8}$$

It is easy to see how, in the perfect pair approximation, when L_b or $L_I = 0$, $q = \mathrm{z}$ meaning that the mean field transmission rate is simply multiplied by the number of nearest neighbors.

Equally, in the mean field context, when L_b or $L_I = 1$, $q = 1$.

From equation (7), it is straightforward to calculate (q_b) for our spatial model, since births are permitted only at the nearest-neighbor interface, and each cell has six adjacent neighbors. As such:

$$q_b = \frac{6}{6*0+1-0} = 6 \tag{9}$$

To this end, we multiplied all mean field birth rates (b=0.025) by 6 to equal .15 in the spatial model.

The dynamics are slightly more complicated in the case of the transmission rate modifier (q_β) because our spatial model allows cells to influence infection up to three 'rings' out from the nearest neighbor, such that each cell is affected by the proportion infectious in a 36-cell vicinity. These dynamics accurately reflect viral transmission, which, even in a plaque assay, can diffuse beyond the immediate neighbor-neighbor boundary, especially in a ten-minute timestep.

As such, we chose to represent transmission processes in the spatial model under assumptions of $L_I = .075$, allowing ~7.5% of transmission to be modeled globally and leading to a less extreme multiplication of the mean field transmission rate than assumed under the perfect pair approximation ($q = \mathrm{z}$) illustrated in equation (9) above. Under these new assumptions, we modify the mean field transmission rate for the spatial context as follows:

$$q_\beta = \frac{36}{36*.075+1-.075} = 9.93 \tag{10}$$

Since this is an approximation and all transitions occur stochastically, we round q_β up to multiply all mean field transmission rates by ten in the spatial context.

Supplementary File 6. Primers for qPCR

Species	Cell Line	Gene	Primer	Sequence	Original Publication
Rousettus aegyptiacus	RoNi/7.1	β-Actin	Fwd	GGCTCCCAGCACAATGAAGA	Biesold *et al.*, 2011
			Rev	GGAGCCGCCGATCCA	Biesold *et al.*, 2011
		IFN-α	Fwd	GAGACTCCCCTGCTGGATGA	Cowled *et al.*, 2011
			Rev	ATAGAGGGTGATTCTCTGGAAGTATTTC	Cowled *et al.*, 2011
		IFN-β	Fwd	CAGCTATTTCCATGAGCTACAACTTG	Biesold *et al.*, 2011
			Rev	TTAACTGCCACAGGAGCTTCAG	Biesold *et al.*, 2011
Pteropus alecto	PaKiT01	β-Actin	Fwd	GGCTCCCAGCACAATGAAGA	Biesold *et al.*, 2011
			Rev	GGAGCCGCCGATCCA	Biesold *et al.*, 2011
		IFN-α	Fwd	GAGACTCCCCTGCTGGATGA	Cowled *et al.*, 2011
			Rev	ATAGAGGGTGATTCTCTGGAAGTATTTC	Cowled *et al.*, 2011
		IFN-β	Fwd	CTCTAGCACTGGCTGGAATGAA	Cowled *et al.*, 2011
			Rev	TGCCCACCGAGTGTCTCA	Cowled *et al.*, 2011

Supplementary File 7. Detailed methods for image and image data processing.

Image Processing.

All image processing and data analysis was carried out in R version 3.6 for MacIntosh (R Core Team 2019). Original images were imported into R and processed via the package EBImage (Pau et al. 2010). Composite images of each well were first split into the 36 or 64-subframes from which they were composed (each subframe represents the visual region of focus for the microscope at the time of imaging). Each subframe was trimmed (to remove border effects), processed individually, and recompiled post-processing into binary form, such that light-colored regions of the original image were assigned a value of 1 (white), and dark regions were assigned a value of 0 (black). In the case of images of GFP-expressing cells, these white regions corresponded to "infectious" cells, while in images of Hoechst-stained nuclei, they indicated live, "uninfected" cells.

Microscope focus was poor for control wells and for subframes early in the time series of each trial before GFP expression became apparent, and the original versions of any such subframes were light gray and grainy. Our image processing code identified these subframes as any which possessed a mean pixel value greater than .25 (a value substantially higher than any subframes in which true GFP-expressing or Hoechst-stained cells were visible) and subsequently converted the entire frame to 0 (black).

All other subframes were processed following thresholding methods that have been previously described by the authors of EBImage (Pau et al. 2010). As a first pass, all pixels excepting the top 25% lightest pixels tallied were converted to 0 (black). Next, each image frame was walked through a series of secondary thresholding steps using if-else statements in R, such that the lightness threshold for "infectious" status was elevated in frames which were lighter overall due to manual variation in imaging and focusing. Processed subframes were then reconstructed into composite binary images, which were manually checked against original images to ensure consistent and reliable results.

Post-processing into binary form, the number of discrete shapes with value of 1 were tabulated within each image, using the max(bwlabel(X)) function in EBimage, to determine a cell count per image, again corresponding to a count of infectious cells for GFP-expressing images and to a count of uninfected cells for Hoechst stain images. All image processing and counting scripts, in addition to the resulting data, are freely available for download at the following FigShare repository: DOI: 10.6084/m9.figshare.8312807.

Image Data processing.

GFP-expressing images were processed and cells counted across the duration of each infection trial, thus generating a time series of infectious cells. For a subset of plates, infection was terminated, and cells were fixed, Hoechst stained, and imaged at periodic intervals across the duration of the time series. Processing of these images thus allowed for construction of a corresponding time series of live, uninfected cells. Because of logistical constraints (i.e. many plates of simultaneously running infection trials and only one available imaging microscope), the time course of imaging across the duration of each trial was quite variable. As such, we fitted a series of statistical models to our raw image data to reconstruct reliable values of the infectious proportion of each well per hour for each distinct trial in all cell line–virus-MOI combinations (Figure 1-figure supplement 2-3).

There was considerable natural variation in initial cell counts across each trial, resulting from subtle differences in the seeding density and growth duration of time until the trial was initiated (when wells were subjectively deemed to have reached "90% confluency"). Baseline cell counts were also different across our three cell lines, which varied substantially in natural size. To correct for this variation, we opted to model the proportion of infectious cell spaces per hour for each well, rather than rely on the raw count data. To this end, we collected the maximum number of live cells counted in susceptible control wells at timepoint 0 and set this count to a rough measure of 100% well occupancy for the cell line in question. Using this method, maximum cell counts were, respectively, 103712, 82308, and 92233 for Vero, RoNi/7.1, and PaKiT01 cell lines, reflecting innate variation in cell sizes. We then converted all cell counts tabulated via our image processing code across the infectious time trials into proportions by dividing the counts by the total number of possible cell spaces for the cell line in question. Though clearly subject to some error, these methods nonetheless maintained internal consistency in our counting methods and generated reasonable time series. We originally experimented with directly tabulating the proportion of infected versus uninfected space in our binary images; however, this approach impaired our ability to generalize across more or less densely seeded trials, as well as trials on cell lines of disparate sizes. As such, we adopted the count-to-proportion methods described here.

To generate an infectious time series of evenly distributed time steps against which to fit our mean field mechanistic model, we next fit a series of statistical models to the proportional data produced from the image processing methods described above. For the GFP-expressing data, we used the mgcv package in R (Wood 2001) to fit generalized additive models (GAMs) in the Gaussian family, with time elapsed (in hours) post infection as a predictor variable for proportion of infectious cells (the response variable). We fit a separate GAM model to each unique cell – virus – MOI combination, incorporating a random effect of well ID (such that each trial was modeled individually), and we fixed the smoothing parameter at k=7 for all trials, as recommended by the package author (Wood 2001). The gam.predict() function was used to return an estimate of infectious proportions per hour across the duration of each time series for each cell-virus-MOI combination.

The uninfected counts from the Hoechst stain data were much less numerous since each count required termination of the infection trial and fixation of cells; by definition, only one data point could be produced per trial. Due to this relative scarcity, we opted to fit a more standard linear regression model, again in the Gaussian family, to these data, rather than using the data-hungry GAM methods employed above. As before, we set time elapsed post infection as the predictor for the Hoechst stain data and produced a unique estimate of the proportion of uninfected cells per hour across the duration of the longest-observed trial. No random effects were included in this model, and the resulting time series were used to estimate natural mortality rates for each cell line, when fit to control well data depicting natural susceptible decline (Figure 1-figure supplement 7).